RSC Advances

PAPER

View Article Online
View Journal | View Issue

Cite this: *RSC Adv.*, 2026, **16**, 4252

Tuning NiCu/AlO(OH) catalysts for optimal glycerol hydrogenolysis to 1,2-propanediol

Asma Ghorbani and Ajay K. Dalai *

Bimetallic NiCu catalysts supported on boehmite (AlO(OH)) with varying Ni and Cu loadings were synthesized through the sequential wet impregnation technique. The AlO(OH) support, characterized by unique properties and a high surface area, was synthesized using a hydrothermal treatment method. Various characterizations on the prepared series of NiCu/AlO(OH) catalysts confirmed the presence of strong Lewis acid sites, and the absence of large agglomeration. Optimization of Ni and Cu loadings on the support achieved the highest catalytic performance with 25 wt% Ni and 15 wt% Cu at 240 °C and 550 psi hydrogen pressure using 4 wt% catalyst loading, resulting in 92.7% 1,2-PD selectivity and 60.3% yield with 65.1% glycerol conversion in 6 h. Further optimization of operating conditions to make 1,2-PD was conducted within the range of temperature, pressure, and catalyst loadings of 200–230 °C, 350–750 psi, and 4–8 wt%, respectively, *via* central composite design using Design Expert software. The 25Ni–15Cu/AlO(OH) catalyst at 6 h was chosen for its high 1,2-PD activity, achieving a high glycerol conversion of 62% with a corresponding 1,2-PD yield of 53.4% (86.0% selectivity of 1,2-PD) under the optimization conditions of 240 °C, 515 psi, and 4.1 wt% catalyst loading, closely aligning with experimental efficiency.

Received 6th October 2025
Accepted 15th December 2025

DOI: 10.1039/d5ra07593a

rsc.li/rsc-advances

1. Introduction

Due to the anticipated depletion of non-renewable energy resources and the adverse environmental effects resulting from increased CO_2 emissions due to their widespread utilization. Many researchers have intensively directed their attention towards the application of biomass-derived feedstock as a promising alternative to conventional petroleum-based fuel. This shift promises to provide long-term solutions to address these challenges. The utilization of biomass for fuel and chemical production aligns with a broader objective of securing a more sustainable and enduring energy future.[1,2] Biodiesel, produced from biomass, has garnered substantial global interest within various industries as it is a viable alternative to traditional petroleum and diesel due to its renewable and environmentally friendly nature.[3,4] Glycerol stands among the top 12 foundational compounds derived from biomass, due to its edible, non-toxic, biodegradable properties, along with its versatile multifunctional structure.[5–7]

Approximately 10% of glycerol is synthesized as a secondary substance when vegetable oils react with methanol or ethanol during the transesterification reaction for biodiesel production. As biodiesel production continues to increase, the primary by-product, crude glycerol, is projected to achieve a global production of 6 million tons by 2025, which can significantly lead to a substantial reduction in its market price.[8,9] The availability of low-cost glycerol in the market provides a wide range of opportunities for its conversion into high-value chemicals, thereby enhancing competitiveness within the biodiesel industry. Among the high-value glycerol transformation pathways, selective catalytic hydrogenolysis is one of the most appealing conversion routes. This process converts glycerol into the desired products of 1,3-propanediol (1,3-PD) and 1,2-propanediol (1,2-PD) by dissociating hydroxyl groups with the addition of hydrogen.[10,11]

1,2-PD serves as an important compound with widespread applications in the production of polyester resins, polyurethanes, agricultural adjuvants, pharmaceuticals, transportation fuel polymers, and plastics. Depending on the purity of 1,2-PD, it can be used as a solvent, hydraulic fluid, and antifreeze agent, as well as for cosmetics and food applications.[12,13] 1,2-Propanediol is mainly formed from glycerol through selective hydrogenolysis reaction process that involves the dehydration of the primary –OH group to acetol on acid (Lewis and/or Brønsted) sites, then subjected to hydrogenation on metallic sites.[14,15] The most employed heterogeneous catalysts for the dehydration–hydrogenation of glycerol for the formation of 1,2-PD are noble metals, including Pd, Ir, Pt, Re, Rh, and Ru, as well as non-noble metals such as Co, Cu, Co, and Ni, either alone or in alloys over various supports.[16–18] Among the non-noble metals, catalysts based on Cu have proven to be highly active in the transformation of glycerol to 1,2-PD,

Catalysis and Chemical Reaction Engineering Laboratories, Department of Chemical and Biological Engineering, University of Saskatchewan, S7N 5A9, Canada. E-mail: akd983@mail.usask.ca; Tel: +1 (306) 966-4771

attributing to their strong performance in cleaving C–O bonds, while showing limited activity in C–C bonds cleavage.[19,20] In addition, Ni-based catalysts are well recognized for their strong hydrogenation ability, which is particularly beneficial in hydrogenolysis reactions.[1] When combined with Cu, a synergistic interaction can further promote the dehydration–hydrogenation pathway, thereby enhancing the conversion of glycerol to 1,2-propanediol. In recent years, mono- and bimetallic Ni–Cu-base catalysts associated with varied supports including Al_2O_3, SiO_2, HY, H-ZSM-5, and H-beta zeolites have been employed for transforming glycerol to 1,2-PD, resulting in certain advancements. Among investigated supports, Al_2O_3 exhibited significant performance towards 1,2-PD. It was also determined that bimetallic Ni–Cu/Al_2O_3 catalysts presented a higher activity in facilitating the formation of 1,2-PD when compared to monometallic catalysts such as Ni/Al_2O_3 and Cu/Al_2O_3 catalysts due to the synergistic interplay between nickel and copper. However, in the case of hydrated form of alumina (boehmite), it was found that the boehmite supported Cu demonstrated the maximum glycerol transformation and selectivity of 1,2-PD in the hydrogenolysis of glycerol among monometallic Cu-based catalysts.[21–26]

Following our recent support-screening study, where 25Ni–10Cu/AlO(OH) achieved 79.5% 1,2-PD selectivity at 90.2% glycerol conversion,[27] we conduct a comprehensive study of the impact of different monometallic (Ni or Cu) and bimetallic compositions (NiCu), different metal loadings, as well as to the optimization of operating conditions for glycerol hydrogenolysis. In this study, nickel and copper were introduced into AlO(OH) *via* a stepwise wet impregnation approach to generate bifunctional catalysts designed for the selective liquid-phase production of 1,2-propanediol. The chemical and textural properties of the synthesized materials were extensively examined using various analytical techniques. In this regard, the AlO(OH) support was synthesized by the one-pot hydrothermal method. Subsequently, a systematic study to gain indepth understanding was conducted on the influence of metal loadings, as well as key process variables, such as pressure, catalyst loading, and temperature on the effectiveness of the catalyst of NiCu-supported catalysts in the hydrogenolysis of glycerol into 1,2-PD using a batch reactor. In addition, catalyst reusability and stability over consecutive reaction cycles were studied to assess long-term activity, which is crucial for practical application and industrial relevance. To the best of our knowledge, this is the first comprehensive research on the synthesized AlO(OH) support and metal loading contents for glycerol hydrogenolysis reported in the literature.

2. Experimental

2.1. Chemicals and materials

The high-purity and analytical grade chemicals were used for all experiments. Nickel(II) nitrate hexahydrate (ACS reagent, purity: 98%) and copper(II) nitrate hemipentahydrate (ACS reagent, purity: 98%) were purchased from Sigma-Aldrich, USA, and used as metal precursors. Glycerol (ACS, purity: 99%), 1,2-propanediol (ACS, purity: 99.5%) were purchased from Thermo Fisher Scientific, USA., aluminum tri-sec butoxide, acetic acid (ACS, 99.7%), and 2-propanol (HPLC, purity: 99.9%) were purchased from Fisher Scientific Canada.

2.2. Preparation of boehmite support and NiCu/AlO(OH) catalysts

The In a typical preparation of the pristine boehmite support, approximately 12.7 g of aluminum tri-sec butoxide liquid was dissolved in 60 ml of 2-propanol under vigorous mechanical agitation for 1 h at 80 °C. Subsequently, an aqueous solution of acetic acid, consisting of 0.102 g of the acid in 2.7 g of deionized water was introduced to the solution and stirred for 10 minutes until a slurry was formed. The slurry was then transferred into a 1 liter Teflon container, tightly sealed, and aged at 100 °C in an oven for 24 h. The resulting solution was filtered to recover the solid products prior to drying at 100 °C in an oven for 3 h. Next, the sample was heated to 600 °C in a muffle furnace for 4 h to remove the template, with a heating rate of 1 °C min^{-1}.

The synthesized AlO(OH) support was used for the preparation of the Ni–Cu catalysts. The catalysts were synthesized by the sequential wetness impregnation technique with an aqueous solution of the modifier metal precursors. The desired amount of nickel nitrate hexahydrate was mixed with water in a beaker. The solution was then agitated for 1 h at room temperature at 150 rpm. To create a homogenous solution, the solution was combined with the support AlO(OH) powder and agitated for 30 min at room temperature. The sample was heated to 450 °C for 5 h at a rate of 1 °C min^{-1} in a furnace muffle after being dried for 3 h at 110 °C.

Similarly, the desired amount of copper(II) nitrate hemi pentahydrate was dissolved in water in a beaker and agitated for 1 h at 25 °C at 150 rpm for the preparation of the supported bimetallic Ni–Cu catalyst. The Ni-supported catalyst was then added to the Cu solution and stirred for 30 min at 25 °C to achieve a homogeneous sample. The obtained sample was dried at 110 °C for 3 h and heated to 350 °C to remove impurities in a muffle furnace for 5 h at a rate of 1 °C min^{-1}. The other batches of NiCu/AlO(OH) catalysts were synthesized using the same procedure. Prior to testing, all catalysts were reduced in a fixed-bed reactor under flow of H_2 at 490 °C for 4 h, then passivated at 25 °C for 1 h in 1% O_2 in N_2.

2.3. Characterization techniques

The catalysts were characterized using a combination of textural, structural, and surface analysis techniques including N_2 adsorption–desorption (BET/BJH), XRD, TEM, SEM-EDS, pyridine-FTIR, XPS, as reported in detail previously.[27]

Thermogravimetric analysis (TGA) was performed using a PerkinElmer Pyris Diamond TG/DTA. Approximately 12 mg of each catalyst sample was heated from 30 °C to 600 °C at a rate of 10 °C min^{-1}, with nitrogen gas flowing continuously during the analysis.

2.4. Catalytic tests for glycerol hydrogenolysis to 1,2-PD

The selective glycerol hydrogenolysis was carried out in a 100 ml stainless steel autoclave equipped with a mechanical stirrer and

temperature controller. The stirring speed and temperature were regulated by the controller. The reactor set up had an inlet valve for gas injection and an outlet valve for venting. For a typical catalytic run, the catalyst sample was reduced at 350 °C for 1 h under H_2 atmosphere. After cooling the reactor content to ambient temperatures, 60 ml of aqueous glycerol solution (20 wt% glycerol) was quickly added to the pressure vessel to prevent aggressive re-oxidation of the reduced catalyst. Subsequently, the vessel was secured in place with tightened nuts and heating jacket followed by purging of the reactor three times with N_2 pressure to remove trapped air in the system prior to experiment. After the standard leakage testing, the reactor was charged with 145 psi H_2 pressure and the temperature and stirring speed were set to 240 °C and 600 rpm, respectively, on the controller. When the temperature reached the desired set point for the reaction, the final H_2 pressure was recorded as ~550 psi and the reaction time was started. The liquid product samples were taken in 2 h interval prior to cooling down of the reactor to ambient conditions and subsequently depressurizing it to atmospheric pressure. The collected liquid products were centrifuged at a speed of 5000 rpm to enhance the separation catalyst particles following by vacuum filtration to recover the liquid products for analysis. The composition of the liquid products was then analyzed using the gas chromatography employing a flame ionization detector (GC-FID) using SupraWAX-280 capillary column, 2-propanol as internal standard and FID detector.

Conversion, selectivity, and yield were calculated according to the following equations:[28,29]

$$\text{Conversion}(\%) = \left(\frac{\text{moles of glycerol reacted}}{\text{initial moles of glycerol}}\right) \times 100\% \quad (1)$$

$$\text{Selectivity}(\%) = \left(\frac{\text{moles of desired product formed}}{\text{moles of all detected products}}\right) \times 100 \quad (2)$$

$$\text{Yield}\ (\%) = (\text{glycerol conversion} \times \text{1,2-PD selectivity}) \times 100\% \quad (3)$$

For catalyst reusability test, the spent catalyst was recovered from the liquid phase after each run, washed three times with deionized water, dried overnight at 100 °C, and then re-reduced under H_2 as previously described before commencing the next reaction cycle.

2.5. Catalytic reaction optimization

The impact of process factors such as reaction temperature, hydrogen pressure, and catalyst loading on the 1,2-propanediol production was studied by the central composite design (CCD) approach. Three independent factors, namely, reaction temperature, hydrogen pressure, and catalyst loading, were varied in the range of 200–240 °C, 350–750 psi, and 2–6 wt%, respectively.

The application of reaction temperature within the range of 200–240 °C appears to offer a favorable balance, as higher temperatures promote the desired hydrogenolysis pathway, albeit excessive heat could trigger undesired side reactions or catalyst deactivation.[21,30] The glycerol transformation and 1,2-PD yield were the response variables in the 20 experimental runs. Coded factors of −1, 0, and +1 were applied to indicate low, centre, and high values, respectively.

The experimental results were investigated using the multiple regression method to establish the quadratic model of the responses. An analysis of variance (ANOVA) was conducted to examine the characteristics of the fitted model employing the statistical software Design-Expert package, version 11.0. Using a response surface modelling tool, the impact of independent parameters on the responses (glycerol conversion (%) and 1,2-PD yield (%)) was determined.

The influence of independent factors on the responses (glycerol conversion (%) and 1,2-PD yield (%)) was determined by a response surface modeling tool.

$$Y = \beta_0 + \sum_{i=1}^{k} \beta_i x_i + \sum_{i=1}^{k} \beta_{ii} {x_i}^2 + \sum_{i>j}^{k} \beta_{ij} x_i x_j \quad (4)$$

where Y is the predicted response, β_0 is a constant, β_i and β_{ii} are first- and second-order constants, β_{ij} is the interaction constant for various factors, and x_i and x_j represent independent variables.

3. Research and discussion

3.1. Catalyst characterizations

The specific surface area, pore volume, and average pore diameter of the pristine AlO(OH) support and corresponding NiCu catalysts are presented in Table 1, and the corresponding N_2 adsorption/desorption isotherms are shown in Fig. 1. As anticipated, the impregnation of various loadings of Ni and Cu on the respective support resulted in a considerable reduction in the surface areas, pore diameters, and pore volumes of the resultant catalysts.

These reductions can be associated with the partial blockage of pores of the support by the deposition of Ni and Cu nanoparticles in the pore channels, possible agglomeration during impregnation or calcinations, and resulting changes in the mesostructure.[31,32]

The surface area of boehmite after loading 25 wt% Ni and 10 wt% Cu on the pristine support evidenced a decrease from 408 $m^2\ g^{-1}$ to 245 $m^2\ g^{-1}$ in the resulting bimetallic catalyst. Only a slight reduction in surface area was observed as copper content increased to 15 wt% in AlO(OH)-supported Ni–Cu

Table 1 Physicochemical properties of different catalysts

Catalysts	S_{BET} ($m^2\ g^{-1}$)	D_{pore} (nm)	V_{pore} ($cm^3\ g^{-1}$)
AlO(OH)	408	12.0	1.56
10Cu/AlO(OH)	275	3.7	0.20
5Ni–10Cu/AlO(OH)	283	4.9	0.39
10Ni–10Cu/AlO(OH)	253	4.8	0.33
15Ni–10Cu/AlO(OH)	272	4.7	0.35
25Ni–10Cu/AlO(OH)	245	3.4	0.18
30Ni–10Cu/AlO(OH)	196	5.1	0.24
25Ni/AlO(OH)	223	4.5	0.29
25Ni–2Cu/AlO(OH)	221	4.5	0.28
25Ni–5Cu/AlO(OH)	210	4.5	0.27
25Ni–15Cu/AlO(OH)	243	4.1	0.26

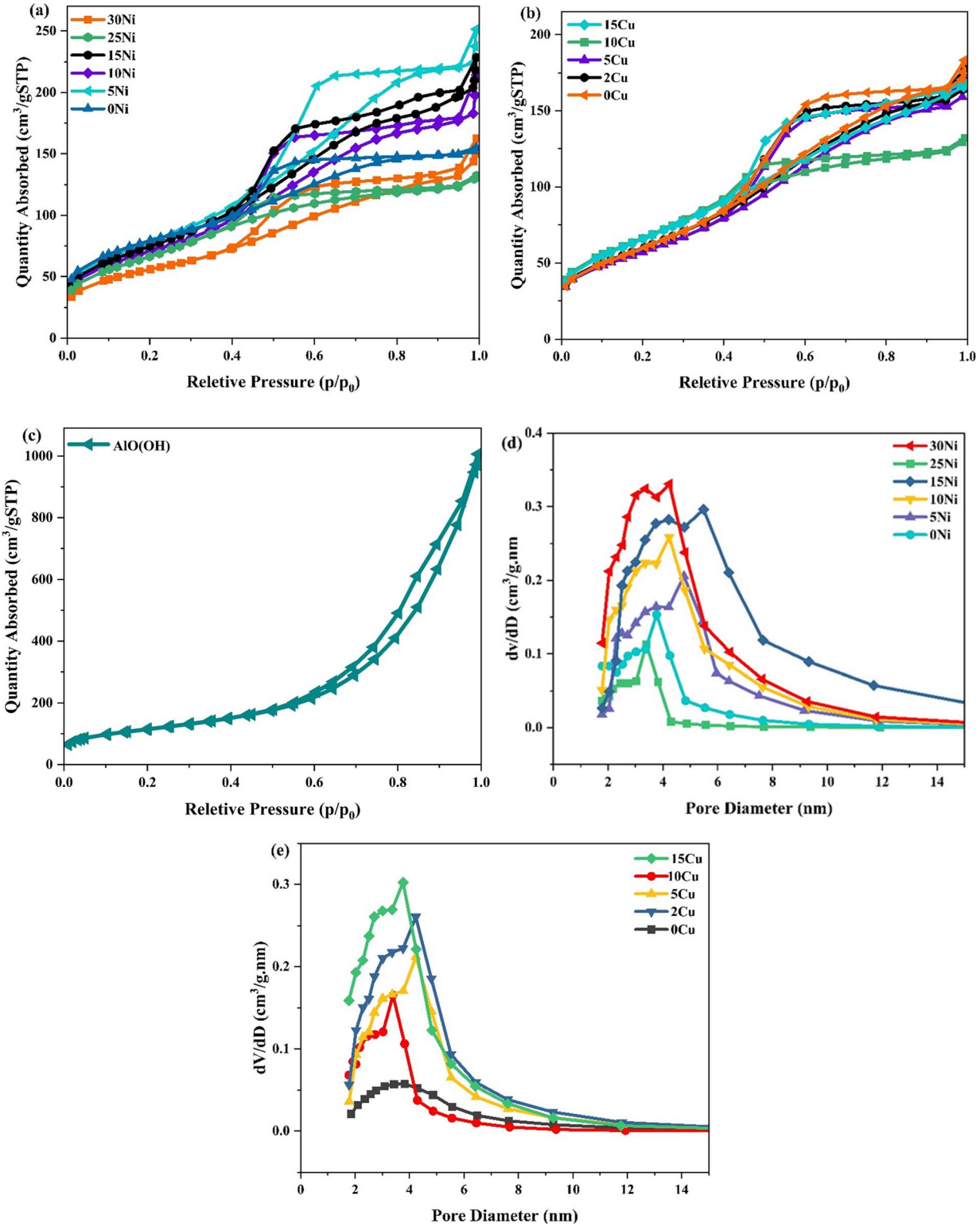

Fig. 1 N_2 adsorption–desorption isotherms: (a) *x*Ni–10Cu/AlO(OH), (b) 25Ni–*y*Cu/AlO(OH), and (c) AlO(OH); pore volume distribution: (d) *x*Ni–10Cu/AlO(OH) and (e) 25Ni–*y*Cu/AlO(OH).

bimetallic catalysts. It is noteworthy to mention that the monometallic 25Ni/AlO(OH) catalyst exhibited a slightly reduced surface area (223 $m^2\ g^{-1}$) compared to the bimetallic Ni–Cu/AlO(OH) catalysts; suggesting that Cu co-presence does not exacerbate pore blockage at moderate levels and may enhance Ni dispersion within the support.[33]

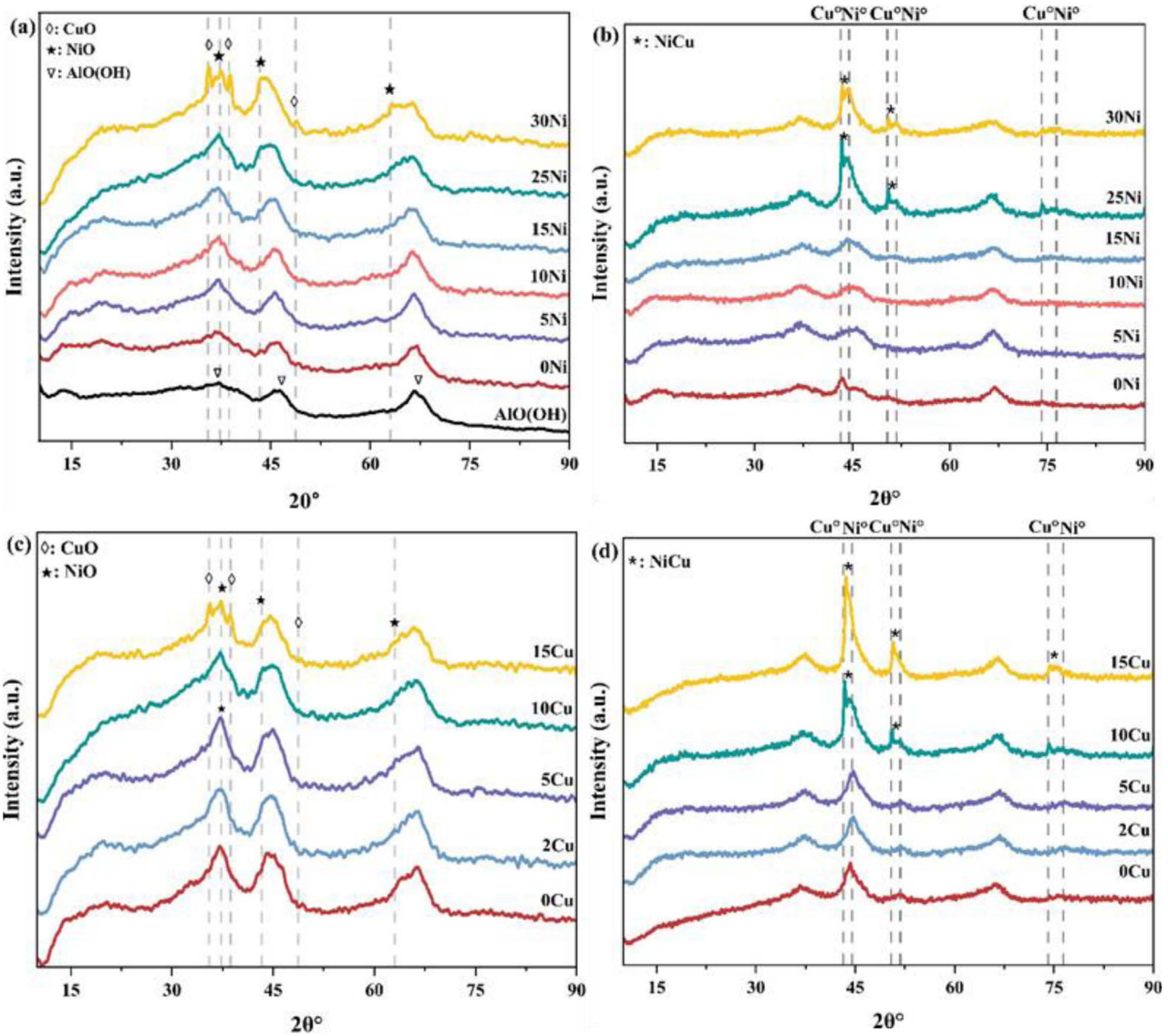

Fig. 2 XRD patterns of Ni loadings in *x*Ni–10Cu/AlO(OH) after (a) calcination (a) and (b) reduction, and Cu loadings in 25Ni–*y*Cu/AlO(OH) after (c) calcination and (d) reduction.

The pore volume of all boehmite-supported catalysts varies from 0.18 to 0.39 $cm^3 g^{-1}$, showing a decrease compared to that of AlO(OH); giving an indication of metal nanoparticles incorporation into the pores during the impregnation step. The BJH diameter of pore channels of all Ni–Cu/AlO(OH) catalysts falls between 3.4–5.1 nm, as confirmed by pore size distribution curves in Fig. 1(c) and (d), while for pure AlO(OH), it was 12 nm. The mesoporous structure in the prepared catalysts could enhance mass transport during the catalytic hydrogenation reaction of glycerol. The significant drop in pore volume and surface area, along with the decrease in diameter of the pore channels, collaborate the observation of incorporation metal precursors during the calcination of the catalyst samples following metal impregnation.

That notwithstanding, all the catalysts exhibited the typical type IV isotherm with H4 hysteresis loop after $p/p_0 = 0.40$, according to IUPAC classification, whereas pristine AlO(OH) displayed H3 hysteresis loop after $p/p_0 = 0.50$. These patterns indicate the presence of mesoporous structures in both pristine AlO(OH) and all synthesized catalysts, as depicted in Fig. 1. After the introduction of Ni and Cu, the hysteresis loop was altered and extended to lower p/p_0 values due to the presence of smaller pores. The position and slope of the hysteresis loop exhibited slight variations, suggesting that the arrangement and consistency of the pore structure have been changed with varying NiCu concentrations.

Fig. 2(a–d) presents the XRD patterns of bimetallic Ni–Cu catalysts supported on AlO(OH), with varying Ni and Cu loadings, for both calcined and *ex situ* reduced samples. The X-ray diffraction patterns of all catalyst samples are very similar. The diffraction peaks corresponding to NiO are expected to be at $2\theta = 37.3°$, 43.3°, and 63.0° (JCPDS No. 44-1159), while those for CuO expect to be identified at $2\theta = 35.5°$, 38.7°, and 48.7° (JCPDS No. 44-0706). Although as shown in Fig. 2(a) and (c), the

Table 2 XRD peak position of (111) Ni–Cu phase, lattice parameters, Ni and Cu compositions of the alloy after *ex situ* reduction at 490 °C

Catalyst	Phase	Lattice a (Å)	2θ (°)	Ni%	Cu%	Particle size (nm) XRD[a]	TEM[b]
25Ni	Ni-rich	3.524	44.5	100.0		5.4	3.2
10Cu	Cu-rich	3.615	43.3		100.0	6.0	3.1
5Ni–10Cu	Cu-rich	3.600	43.5	15.9	84.1	5.3	
10Ni–10Cu	Cu-rich	3.584	43.7	33.2	66.8	5.4	
15Ni–10Cu	Ni-rich	3.569	44.2	50.3	49.7	6.1	
25Ni–10Cu	Cu-rich	3.577	43.8	42.6	57.4	7.6	3.8
30Ni–10Cu	Ni-rich	3.554	44.1	67.0	33.0	6.7	
25Ni–2Cu	Ni-rich	3.538	44.3	83.9	16.1	5.6	
25Ni–5Cu	Ni-rich	3.546	44.2	75.5	24.5	5.8	
25Ni–15Cu	Cu-rich	3.592	43.6	24.6	75.4	7.8	3.1

[a] Calculated from Vegard's law for *ex situ* reduced catalysts. [b] Average particle size from the histogram.

diffraction patterns of calcined catalysts indicate broad and low-intensity NiO/CuO reflections for all *x*Ni–*y*Cu/AlO(OH) catalysts, this behaviour is consistent with the presence of small nanocrystalline NiO and CuO domains rather than large, well-crystallized particles. A slight increase in peak intensity was observed for the catalyst with higher Ni content (30Ni–10Cu/AlO(OH)), possibly indicating a slight increase in the crystallinity of the NiCu phase compared others. In addition, Scherrer analysis of the NiO and CuO reflections in the calcined catalysts gives crystallite sizes below ~4 nm, confirming that the oxide phases are initially present as nanosized domains on the AlO(OH) support; such small crystallites are expected to result in more catalytic accessibility, which could be beneficial for hydrogenolysis of glycerol to 1,2-propanediol.[34] After reduction, XRD patterns (Fig. 2(b) and (d)) showed that both NiO and CuO were completely reduced, with formation of Ni–Cu peaks at intermediate positions between Cu^0 (peaks at 43.3°, 50.5° and 74.2°, JCPDS 04-0836) and Ni^0 (peaks at 44.5°, 51.9° and 76.4°, JCPDS 04-0850).[35,36]

These findings indicate the formation of Ni–Cu alloys, attributed to the successful incorporation of Cu atoms into the Ni lattice in bimetallic catalysts. The primary Ni–Cu peaks are observed at 2θ values of approximately 43.5–44.3° (111 reflection), 50.5–50.8° (200 reflection), and 74.6–74.8° (220 reflection), consistent with a face-centered cubic (FCC) structure typical of Ni–Cu alloys. This observation aligns with previous studies on NiCu bimetallic catalysts.[35–38] The characteristic diffraction peak of Ni^0 at 44.5° was observed in the reduced monometallic 25Ni/AlO(OH) catalyst (Fig. 2(c)), while the diffraction peaks at 43.3° attributable to metallic Cu^0 presented in reduced 10Cu/AlO(OH) (Fig. 2(b)).

The formation of NiCu alloys in the reduced catalysts is a critical factor influencing the catalytic performance in glycerol hydrogenolysis to 1,2-PD.[39] Vegard's law ($\alpha_{Ni_xCu_{1-x}} = x \times \alpha_{Ni} + (1 - x) \times \alpha_{Cu}$) was employed to quantify the alloy composition, assuming a linear relationship between the lattice parameter and the composition of a solid solution.[36] By analyzing the shift in the (111) reflection peak positions (43.4–44.3°), the Ni% and Cu% content in the NiCu alloys were determined and presented in Table 2. A peak shift closer to 43.3° (pure Cu^0) indicates a Cu-rich alloy, whereas a shift toward 44.5° (pure Ni^0) suggests Ni enrichment. In this study, the calculated compositions show that the alloys vary from Cu-rich to Ni-rich depending on the initial metal loadings. For instance, the 25Ni–10Cu/AlO(OH) catalyst shows a peak at ~43.8° with a lattice parameter of 3.577 Å, corresponding to a $Ni_{0.426}Cu_{0.574}$ alloy and confirming a Cu-rich phase. Similarly, the 25Ni–15Cu catalyst exhibits a further shift toward Cu, with a 2θ value of 43.6° and a lattice parameter of 3.592 Å, showing a $Ni_{0.246}Cu_{0.754}$ composition.

In contrast, the 15Ni–10Cu/AlO(OH) catalyst exhibits a peak at 44.2° with a lattice parameter of 3.569 Å, corresponding to a $Ni_{0.503}Cu_{0.497}$ alloy and reflecting a Ni-rich phase. These compositional variations indicate that the alloy phase can be tuned by adjusting the Ni and Cu loadings.[40]

The crystallite sizes of the NiCu alloys in the reduced catalysts were calculated using the Scherrer equation and are summarized in Table 2.

The calculated values range from approximately 5 nm to 8 nm, which are somewhat larger than the crystallite sizes of the calcined oxides, indicating moderate particle growth during reduction at 490 °C. However, the metallic phase remains in the nanometre range, indicating that Ni–Cu is relatively uniformly dispersed on the AlO(OH) support. In particular, the Cu-rich catalysts, such as 25Ni–10Cu/AlO(OH) and 25Ni–15Cu/AlO(OH), combine 5–8 nm Ni–Cu crystallites with balanced Ni/Cu ratios. These structures are expected to improve both activity and selectivity toward 1,2-propanediol. This trend agrees with previous reports showing that Cu-rich Ni–Cu alloys promote selective C–O bond hydrogenolysis while limiting unwanted C–C bond cleavage.[41]

TEM images at magnifications of 50 and 100 nm, along with the corresponding particle size distributions of the AlO(OH)-supported Ni–Cu catalysts, are presented in Fig. 3 and summarized in Table 2. At higher magnification (50 nm scale), the dark-contrast domains correspond to reasonably finely distributed Ni- or Cu-containing oxide particles anchored on the boehmite platelets, while the 100 nm images highlight that these nanoparticles are homogeneously distributed over the support without formation of large (>10 nm) crystallites.[42,43] AlO(OH) supports are well known to stabilize highly dispersed transition-metal nanoparticles through strong metal–support interactions, their high surface area, mesoporosity, and similar morphologies have been reported for Ni-based catalysts on boehmite-derived alumina by Zheng *et al.*[43]

The average particle size for Ni and Cu species in both mono- and bimetallic catalysts is approximately 3 nm, within a range of 1–5 nm. These observations confirm that all catalysts samples contain nanosized metal oxide particles without significant agglomeration, and that mono- and bimetallic formulations maintain comparable particle-size characteristics. Particle sizes in this range are typical for NiCu-based catalysts and are frequently attributed to improved hydrogenation activity.[44,45] Thus, although the absolute values are semi-quantitative, the TEM analysis indicates that all these mono- and bimetallic catalysts contain very small, uniform Ni–Cu oxide nanoparticles on AlO(OH).

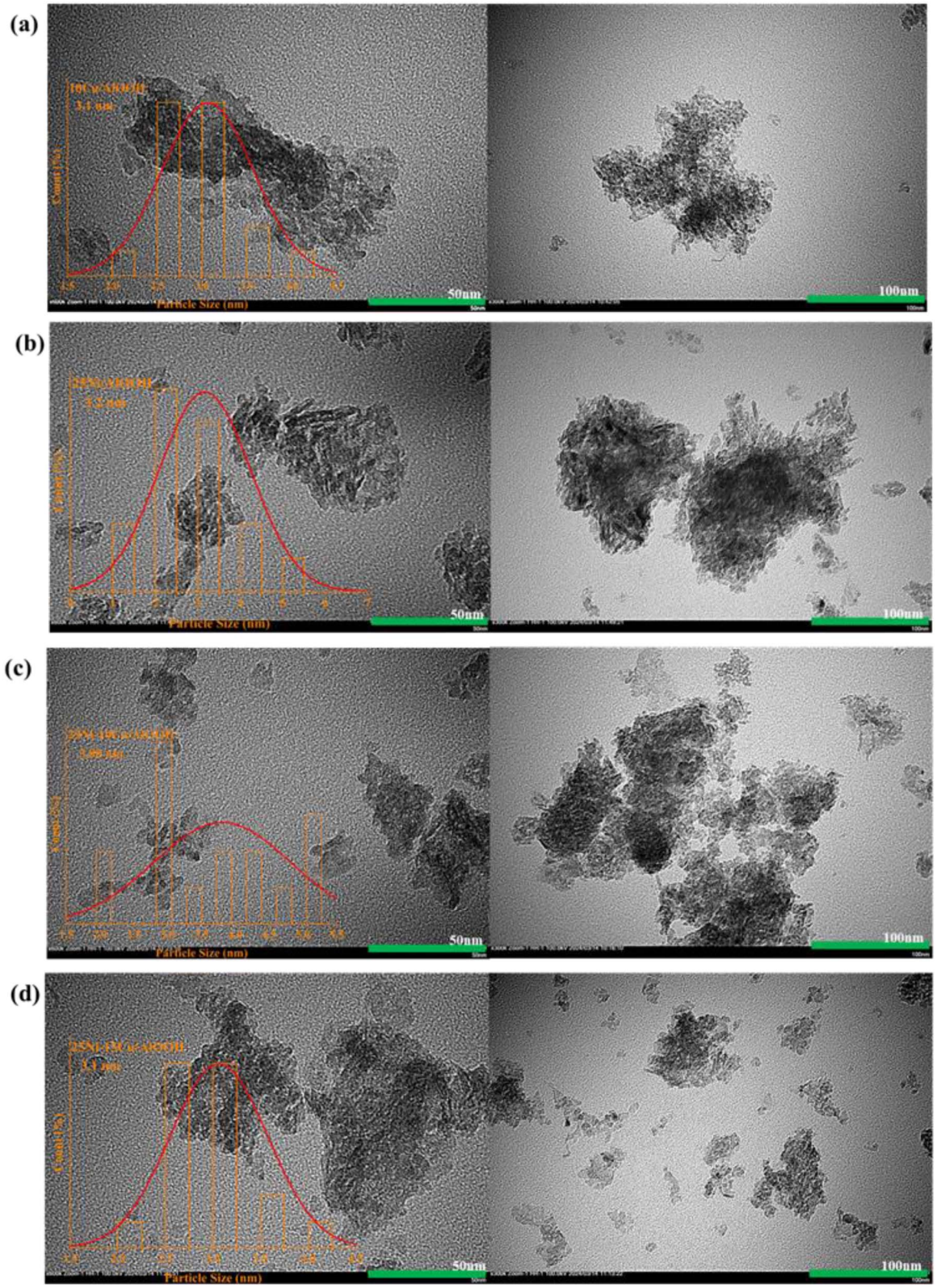

Fig. 3 TEM images of (a) 10Cu/AlO(OH), (b) 25Ni/AlO(OH), (c) 25Ni–10Cu/AlO(OH), and (d) 25Ni/15Cu/AlO(OH) catalysts at 50 nm and 100 nm, and average particles size distribution.

It should be noted that, due to the similar lattice parameters and atomic numbers of Ni and Cu, as well as the magnifications (50 and 100 nm) and the relatively low accelerating voltage used (100 kV), the contrast between Ni- and Cu-rich domains and the AlO(OH) matrix is modest, and overlapping aggregates lead to somewhat blurred particle boundaries. TEM primarily provides

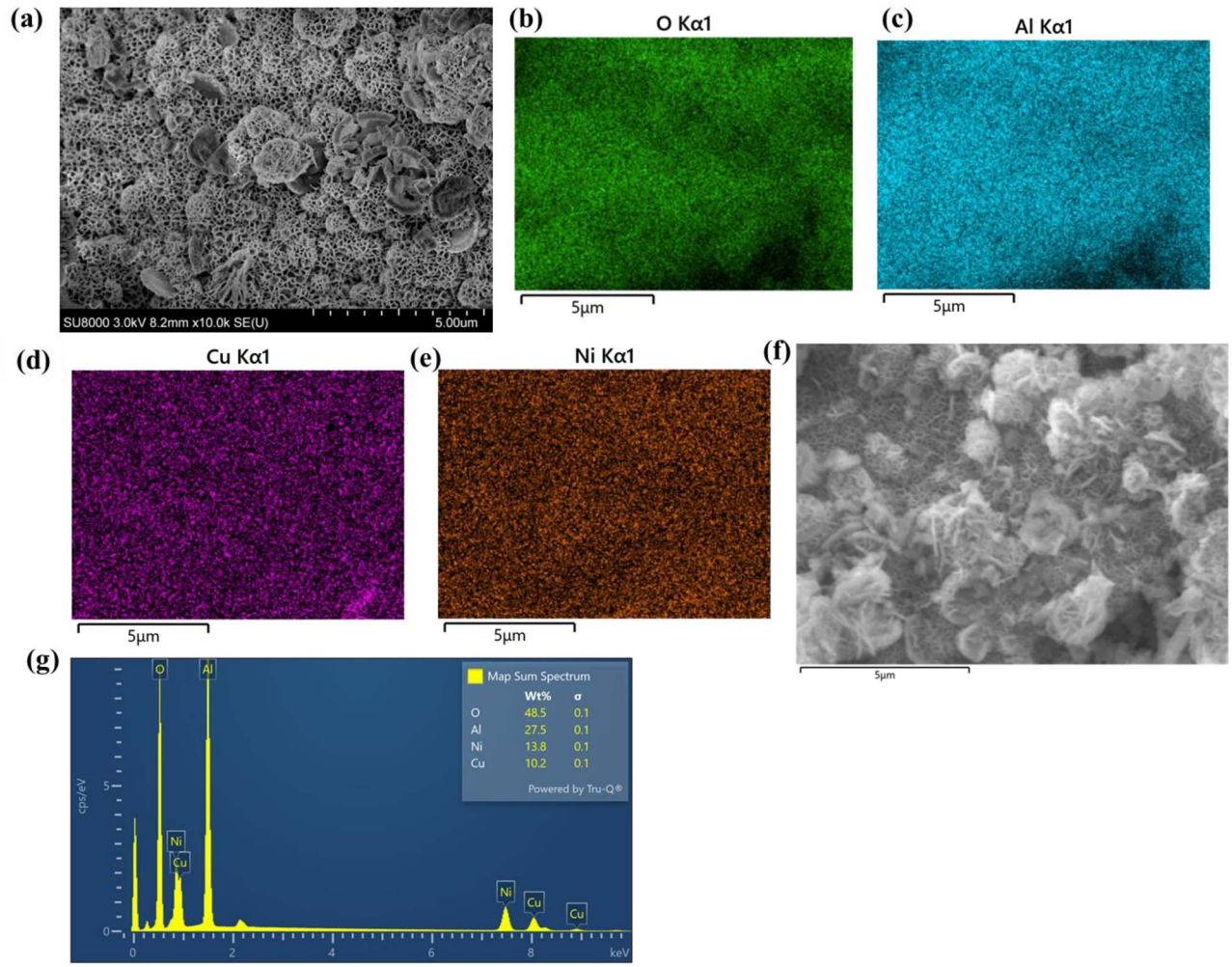

Fig. 4 (a) SEM image and (b–g) corresponding EDS elemental maps of the bimetallic 25Ni–15Cu/AlO(OH) catalyst after calcination.

qualitative and semi-quantitative information on the particle size, shape, and dispersion of metal species within the support. Consequently, in this study, TEM in this work is used mainly to demonstrate the absence of large agglomerates and to estimate the order of magnitude of the particle size, rather than to provide an exact metal dispersion.[41,46] Comparable TEM-based particle sizes and dispersion behaviours for Ni–Cu catalysts on alumina-type supports have been reported by Vance *et al.*,[47] Zhao *et al.*,[48] Shi *et al.*,[49] and Zhu *et al.*[50] The uniform nanostructure observed here aligns with the XRD results (Fig. 2 and Table 2), indicating finely divided metal oxide phases on the AlO(OH) support.

The SEM-EDS was employed to examine the morphology and elemental composition of the 25Ni–15Cu/AlO(OH) catalyst, identified as the most effective in glycerol hydrogenolysis to 1,2-PD, as presented in Fig. 4(a–g). The SEM image at a 5 μm scale (Fig. 4(a)) exhibits a highly porous, irregular structure composed of interconnected particles.[51] This porous, flower-like morphology provides a high surface area of 243 $m^2\ g^{-1}$, enhancing the accessibility of active sites for glycerol hydrogenolysis and thereby contributing to the high activity of catalyst. EDS elemental mapping (Al K_{α_1}, O K_{α_1}, Cu K_{α_1}, and Ni K_{α_1}) of 25Ni–15Cu/AlO(OH) (Fig. 4(c–e)) demonstrates a uniform distribution of Al, O, Ni, and Cu over the catalyst surface at the 5 μm scale, confirming the relative uniform dispersion of active metal species on the AlO(OH) support, which is essential for optimal catalytic activity.

In Fig. 4(f and g), the EDS spectrum shows the elemental composition of the 25Ni–15Cu/AlO(OH) catalyst as O (48.5 wt%), Al (27.5 wt%), Ni (13.8 wt%), and Cu (10.2 wt%). The high O and Al contents are consistent with the AlO(OH) support. The EDS elemental mapping confirms a homogeneous distribution of Al and O across the catalyst, indicating a well-preserved and stable support. The ratio of Ni/Cu (15.1/10.3 = 1.35) reasonably aligns with the intended 25Ni–15Cu composition (25/15 = 1.67), confirming successful incorporation of both metals into the catalyst. This balanced Ni/Cu ratio and uniform distribution of Ni and Cu is essential for the formation of a bimetallic NiCu alloy, as further supported by TEM and XRD measurements.

The nature of acid sites (Lewis and/or Brønsted) and strength of acid sites of the prepared catalysts play a critical role in the selective hydrogenolysis of glycerol, generally characterized by the pyridine adsorbed FTIR (Py-FTIR) patterns. The Py-FTIR patterns of different AlO(OH) supported monometallic and

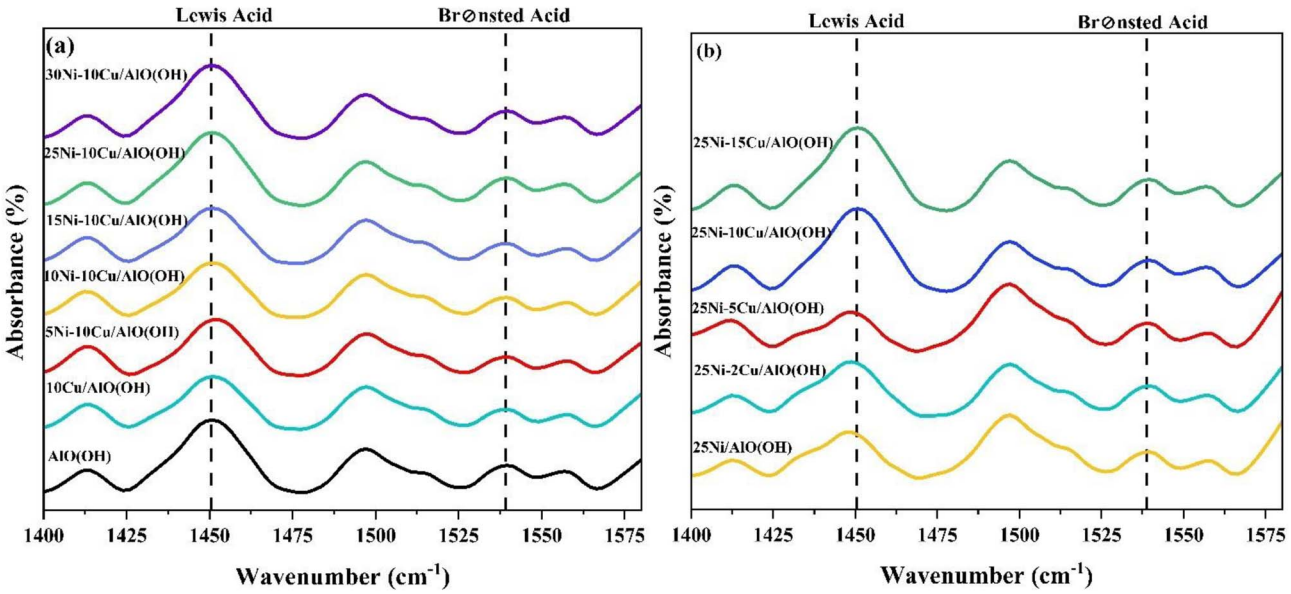

Fig. 5 Pyridine adsorbed FTIR patterns of different loadings of Ni in (a) *x*Ni–10Cu/AlO(OH) and different loadings of Cu in (b) 25Ni–*y*Cu/AlO(OH).

bimetallic catalysts are presented in Fig. 5. The peak areas corresponding to Brønsted and Lewis acid sites, derived from the Py-FTIR spectra, are summarized in Table S1, providing quantitative information on the relative acidity and distribution of acid site types. An adsorption band at 1450 cm^{-1} is ascribed to the interaction between pyridium ions and Lewis acid sites, and a relatively weak adsorption band at 1540 cm^{-1} is ascribed to the interaction between pyridine and Brønsted acid sites, suggesting a predominant presence of Lewis acid sites. The intensity of Lewis acid sites is beneficial for the initial conversion of glycerol to an intermediate product (acetol) *via* the dehydration step, which would be further converted to 1,2-PD. In fact, the dehydration reaction relies on the acidic functionality of the support, whereas metallic properties are required for the hydrogenation or dehydrogenation steps. Fig. 5(a) indicates that introducing Ni loading from 5 to 30 wt% progressively increases the intensity of Lewis acid sites while the intensity of Brønsted band remains low. The inherent amphoteric nature of AlO(OH) possesses Brønsted sites from Al–OH groups and moderate Lewis acidity from Al^{3+} cations.

Incorporation of Ni, particularly at higher loadings (30Ni–10Cu/AlO(OH)), enhances Lewis acidity, likely due to the formation of Ni^{2+} species or Ni–Al mixed oxide phases that introduce additional coordinatively unsaturated sites.[52] In Fig. 5(b), at constant 25 wt% Ni loading, increasing Cu loading from 2 to 15 wt% further enhance the intensity of Lewis acid sites with a modest increasing of the Brønsted acidity, suggesting Cu primarily tunes Lewis acidity, with a minor Brønsted contribution possibly arising from Cu-induced changes in surface hydroxyls. These observations highlight the importance of maintaining a proper balance between the dual catalytic functions, involving acid and metal sites is important for glycerol hydrogenolysis. In conclusion, the variance in glycerol hydrogenolysis activity may not be predominantly attributed to the acidity of the catalyst.[53]

It is widely recognized that the oxidation state of the active site significantly affects its catalytic performance, particularly in metallic-based catalysts. XPS spectroscopy was employed to analyze the surface elemental composition, and the chemical environment of the elements present on the surface of AlO(OH)-supported NiCu.

The catalysts were pre-treated by reduction at 490 °C under a flow of H_2 to activate the metallic sites, followed by passivation with a 1% O_2 in N_2 flow at room temperature to stabilize the surface against further oxidation during *ex situ* transfer to the XPS instrument. Consequently, the resulting spectra represent the near-surface states of passivated, reduced catalysts, rather than the fully metallic surfaces present under H_2 flow. While this *ex situ* approach can lead to partial re-oxidation, it enables evaluation of catalyst stability and the post-reduction electronic environment, information directly relevant to performance in glycerol hydrogenolysis to 1,2-propanediol.[20]

Ni $2p_{3/2}$ spectra (as presented in Fig. 6(a)) show two main peaks and a shake-up satellite at 853.1–853.9 eV (Ni^0), 855.7–856.3 eV (Ni^{2+}, likely NiO or $Ni(OH)_2$-like), and 861.7–862.4 eV, respectively, with $Ni^0/(Ni^0 + Ni^{2+})$ ratios of 0.12–0.17 across the catalyst series (Table S2), indicating that the near-surface region is dominated by oxidic Ni^{2+} while a smaller fraction of metallic Ni is retained after passivation. These values match literature-reported positions for Ni^0 and Ni^{2+} in supported Ni catalysts.[37,39,54] Such partial re-oxidation and persistence of Ni–Al–O species are typical for *ex situ* XPS of Ni/alumina-type catalysts reduced at 400–500 °C.[39,55]

The slight but consistent shifts observed in the Ni $2p_{3/2}$ binding energies support the presence of electronic interactions between Ni, Cu and the AlO(OH) support. In the bimetallic catalysts, the Ni^0 peak is marginally shifted toward higher binding energies relative to monometallic 25Ni/AlO(OH), indicating a more electron-deficient Ni environment. This behavior aligns with partial Ni–Cu alloy formation and modified metal–

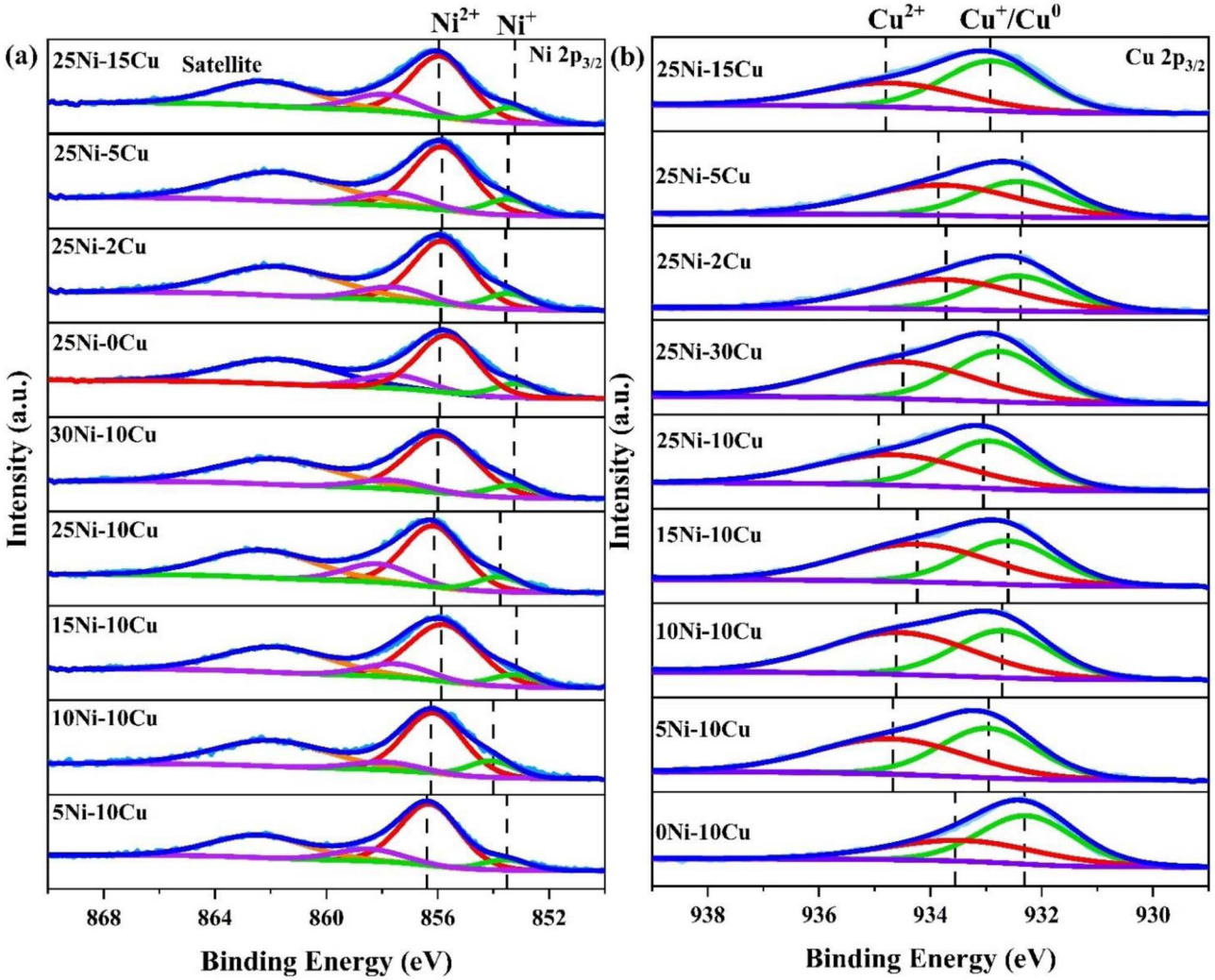

Fig. 6 High-resolution XPS spectra of (a) Ni $2p_{3/2}$ and (b) Cu $2p_{3/2}$ for *ex situ* reduced *x*Ni–*y*Cu/AlO(OH) catalysts at 490 °C.

support interactions commonly observed in Ni–Cu catalyst systems.[20,56–58] For 25Ni–10Cu, the BE shift to higher binding energy in Ni binding energies suggests electron-poor Ni due to Cu-rich composition, lattice strain, and support interactions on boehmite. This aligns with XRD data (Table 2) indicating a Cu-rich alloy (42.6% Ni, 7.6 nm crystallite sizes). In contrast, 30Ni–10Cu is Ni-rich alloy (67% Ni) with larger crystals (~6.7 nm), so alloy effects are weaker and Ni binding energy decreases again. In all cases, however, the presence of metallic Ni^0 species remains essential for catalytic performance, as Ni^0 provides the sites required for H_2 activation and C–O bond hydrogenolysis during the conversion of glycerol to 1,2-PD.[54]

As presented in Fig. 6(b), The Cu $2p_{3/2}$ spectra reveal peaks for reduced Cu species (Cu^0/Cu^+) and oxidized Cu (Cu^{2+}), with BEs ranging from 932.2 to 932.9 eV for Cu^0/Cu^+ and 933.4–934.7 eV for Cu^{2+}, with the $Cu^0/(Cu^0 + Cu^{2+})$ ratio ranging from 0.42 to 0.59 (Table S2). The highest value $Cu^0/(Cu^0 + Cu^{2+})$ ratio is observed for monometallic 10Cu/AlO(OH) (0.59), whereas the other bimetallic Ni–Cu catalysts show intermediate values. Among them, 25Ni–10Cu/AlO(OH) and 25Ni–15Cu/AlO(OH) maintain relatively high metallic Cu fractions (0.49 and 0.51, respectively). Upon introduction of Ni, the Cu $2p_{3/2}$ peaks for both Cu^0/Cu^+ and Cu^{2+} shift by ~0.3–0.6 eV to higher binding energies, suggesting a slightly more electron-deficient Cu environment consistent with electronic interaction and partial formation of Ni–Cu alloy.[59,60]

XPS-derived surface states are directly relevant to glycerol hydrogenolysis. Broad evidence indicates that Cu^0/Cu^+ sites favor glycerol dehydration to acetol, whereas Ni^0 promotes hydrogenation of these intermediates to 1,2-PD; by contrast, excess Ni^{2+} or Cu^{2+} suppresses activity and can divert pathways. Comparative studies of mono- *versus* bimetallic catalysts further show that electronically interacting Ni–Cu ensembles enhance 1,2-PD productivity and selectivity.[41,61,62] These findings indicate that precise tuning Ni–Cu composition and electronic structure produces surface ensembles that most effectively promote selective hydrogenolysis to 1,2-PD.

3.2. Catalytic performance

A comparative analysis of the hydrogenolysis activity of glycerol into 1,2-PD over a series of AlO(OH)-supported bimetallic Ni–Cu

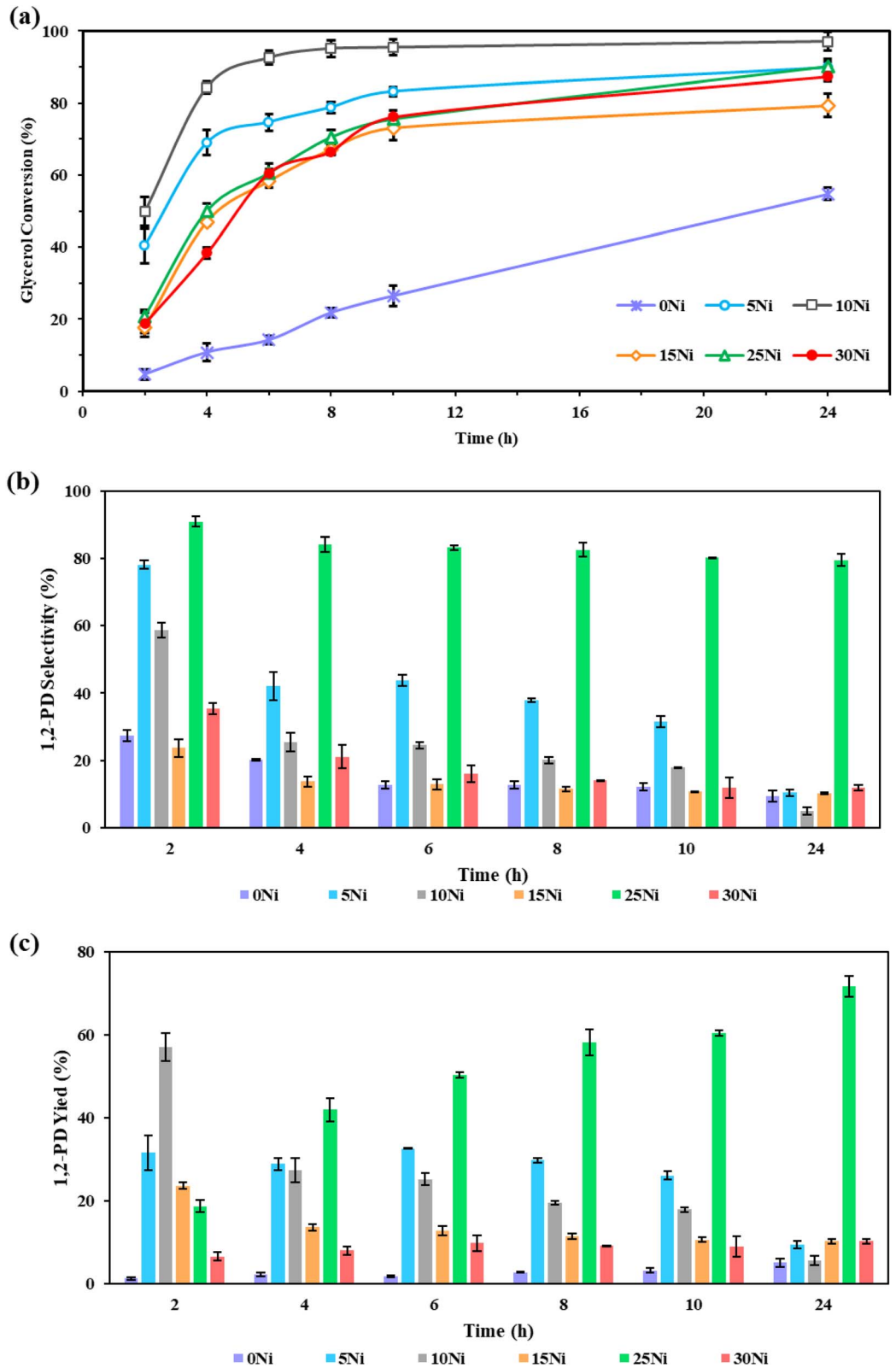

Fig. 7 Effect of Ni loading on *x*Ni–10Cu/AlO(OH) in glycerol hydrogenolysis to 1,2-propanediol at 240 °C, 550 psi H_2, 600 rpm, 4 wt% catalyst loading, and 20 wt% glycerol solution. (a) Glycerol conversion, (b) 1,2-PD selectivity, and (c) 1,2-PD selectivity.

catalysts was evaluated in the liquid phase using a batch reactor. Hydrogenolysis of glycerol occurs *via* dehydration on the acid sites of the supports to generate intermediates (acetol and 3-hydroxypropionaldehyde (3-HPA)) and subsequent hydrogenation to yield propanediols (1,2-PD and 1,3-PD) on metal sites. The synergistic impacts of active metals and acid

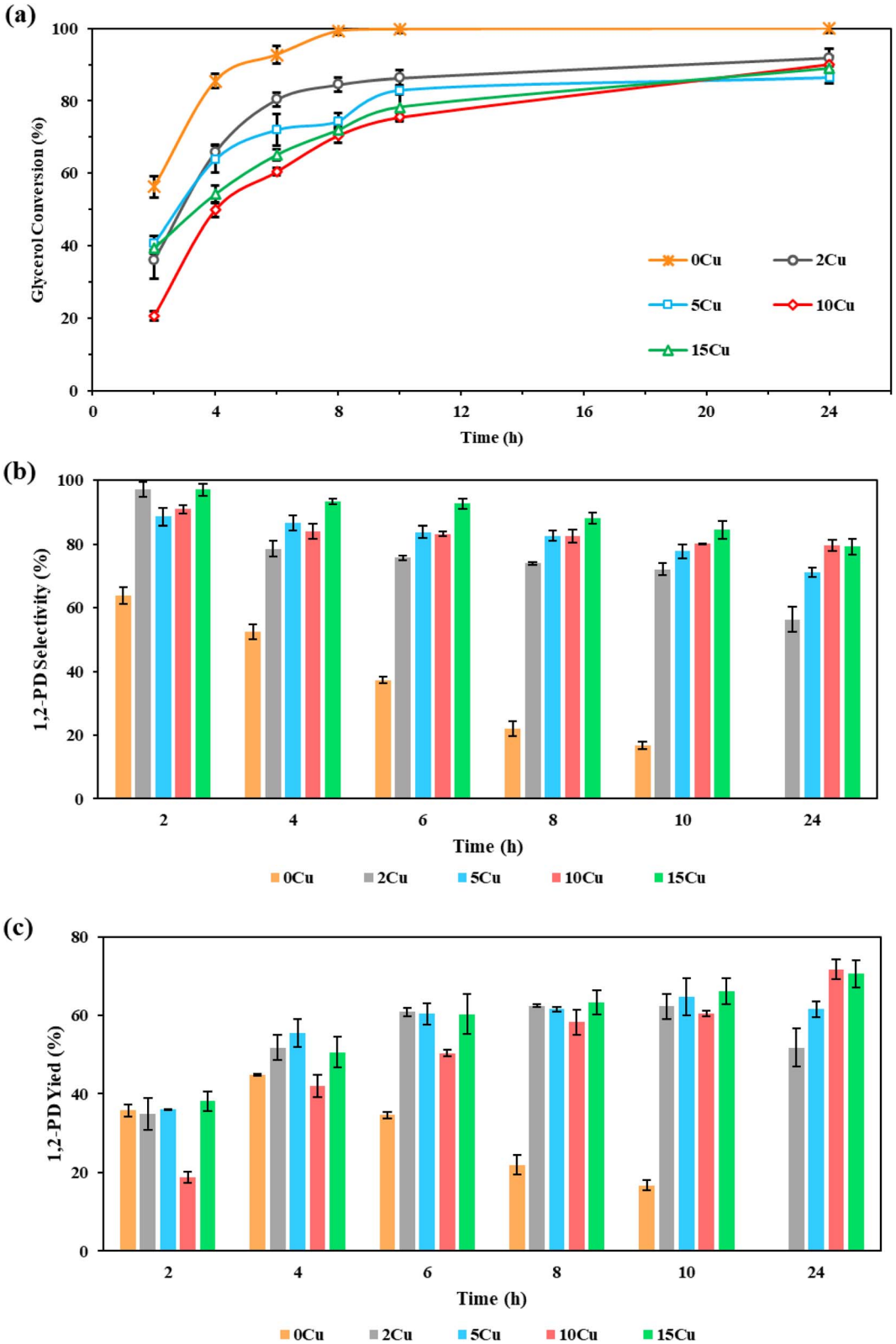

Fig. 8 Effect of Cu loading on 25Ni–*y*Cu/AlO(OH) in glycerol hydrogenolysis to 1,2-propanediol at 240 °C, 550 psi H_2, 600 rpm, 4 wt% catalyst loading, and 20 wt% glycerol solution. (a) Glycerol conversion, (b) 1,2-PD selectivity, and (c) 1,2-PD selectivity.

sites have been proven to significantly impact the catalytic activity of glycerol hydrogenolysis. A balanced distribution of acid and metal sites also facilitates the achievement of remarkable reaction performance.[63] Preliminary transport analysis (stirring-rate variation and Weisz–Prater criterion, $\varphi \leq 1$) confirmed that intraparticle and external mass-transfer

limitations are negligible under the applied reaction conditions. Therefore, the effects of different metal loadings in metal–acid bifunctional catalysts were studied.

The main product obtained was 1,2-propanediol, and all the catalysts exhibited appreciable conversion and selectivity for 1,2-PD during glycerol hydrogenolysis. To favor the formation of the desired product and minimize the side reactions of glycerol hydrogenolysis, catalyst compositions and reaction parameters were systematically optimized to achieve high transformation and 1,2-PD selectivity.

3.2.1. Ni loading screening. To gain an insight into the efficiency of the reaction towards 1,2-PD, the impact of Ni loading in the range of 0–30 wt% over AlO(OH)-supported Ni–Cu catalysts at constant copper loading of 10 wt% was studied under the reaction conditions of 240 °C and 550 psi for a duration of 24 h, as reported in Fig. 7. The conversion of glycerol progressively increased with reaction time from 2 to 24 h for all Ni loadings, from 4.6% over monometallic 10Cu/AlO(OH) (0 wt% Ni) after 2 h to 97.0% for 10 wt% Ni after 24 h (Fig. 7(a)). It can be noted that an extended contact time enhanced more interactions between the reactant molecules and the active sites of the catalyst through diffusion, resulting in an increased glycerol conversion. The low glycerol conversion by the catalyst containing no Ni (10Cu/AlO(OH)) over the same reaction interval indicated that Cu alone provides only limited hydrogenation capability or may be less effective in activating hydrogen necessary for the hydrogenolysis reaction. Moreover, as the Ni loadings increased from 0–10 wt%, an incremental rise in the glycerol conversion can be observed; however, further increasing Ni content from 15 to 30 wt% as not beneficial due to possible agglomeration of Ni loadings leading to negligible glycerol conversion. In other words, the interplay between Ni and Cu sites is critical. Cu provides sites that facilitate C–O bond dissociation, directing the reaction pathway towards 1,2-PD, while Ni supplies the hydrogenation capacity. Properly balanced, this synergy guides the reaction selectively towards the desired product (1,2-PD). Furthermore, as presented in Fig. 7(b), the 25 wt% Ni-loaded 10Cu/AlO(OH) catalyst exhibited the best performance with enhanced selectivity and yield with respect to the desired product (1,2-propanediol) as compared to the other Ni loadings under the existing reaction conditions. Moreover, as can be seen from Fig. 7(c), the yield of 1,2-PD over the 25Ni–10Cu/AlO(OH) catalyst gradually increased with increasing reaction time up to 24 h, with a 1,2-PD yield of 71.7% with a selectivity of 79.5%. Though, a highest glycerol conversion of 97.0% was achieved for the 10 wt% Ni-loaded 10Cu/AlO(OH) catalyst, the selectivity and yield declined to 5.6% and 5.5% after a reaction time of 24 hours. Additionally, monometallic 10Cu/AlO(OH) (0 wt% Ni) exhibited the lowest activity and selectivity towards 1,2-PD at almost all reaction times. With the increase in Ni loading to 30 wt%, the 1,2-PD selectivity and yield declined. The 30Ni–10Cu/AlO(OH) catalyst exhibited a lower metallic Cu fraction compared to the other formulations, as confirmed by the XPS pattern. As mentioned before, varying loadings of bimetallic NiCu on AlO(OH) exhibited smaller pore sizes, uniform distribution, and reduced particle sizes, collectively contributing to increased glycerol conversion and 1,2-PD selectivity. However, a higher loading of Ni at 30 wt% in 30Ni–10Cu/AlO(OH) may increase the likelihood of agglomeration and result in a smaller-pore catalyst. As can be observed in the XRD pattern in Fig. 2(a), the 30Ni–10Cu/AlO(OH) catalyst displays relatively more intense peaks compared to other NiCu/AlO(OH) loadings. Under such circumstances, despite possessing a large number of both metal and acid active sites, lower transformation rate of glycerol and 1,2-PD selectivity may be obtained. This phenomenon may arise from the restricted diffusion of reactants and products within the narrow pores of the 30wt% Ni–10Cu/AlO(OH) catalyst. The slow transportation of glycerol molecules within these pores results in a decreased rate of glycerol conversion.

Therefore, it can be concluded that 25Ni–10Cu/AlO(OH) catalyst exhibited the highest Lewis acidity among the Ni-loading series at fixed 10 wt% Cu and provided sufficient active metal sites essential for facilitating the hydrogenation reaction of acetol to 1,2-propanediol during the hydrogenolysis of glycerol. The results suggest that 25 wt% Ni on the *x*Ni–10Cu/boehmite catalyst was adequate for achieving maximum selectivity and yield of 1,2-PD, which could potentially be attributable to the synergistic impacts of metal species incorporated by impregnation and the Lewis acidic sites of boehmite. Consequently, subsequent experiments were conducted using the optimal 25Ni–10Cu/AlO(OH) catalyst.

3.2.2. Cu loading screening. The influence of varying Cu loading in the range of 0–15 wt% on the catalytic performance of glycerol hydrogenolysis over the 25Ni–*y*Cu/AlO(OH) catalysts was examined for 24 h, as presented in Fig. 8(a–c). Interestingly, at 0% Cu loading, the 25Ni/AlO(OH) catalyst demonstrated the maximum glycerol conversion of 99.8% at 10 h reaction time, However, it exhibited a low selectivity of 16.8% after 10 hours. Evidently, introducing a small quantity of Cu (2 wt%) onto 25Ni/AlO(OH) catalyst significantly enhanced the selectivity of 1,2-propanediol (as shown in Fig. 8(b)) as well as 1,2-propanediol yield (Fig. 8(c)) up to 97.1% and 34.8%, respectively at a 35.9% glycerol conversion (Fig. 8(a)) within the initial 2 hours. This suggests that metallic Cu plays a promotional role in glycerol hydrogenolysis, contributing to the hydrogenation of intermediates leading to 1,2-propanediol. It was evident that prolonged contact time enhanced glycerol conversion by allowing more glycerol to react by diffusion with the catalyst active sites.

The glycerol conversion decreased from ~100% to ~89% as the Cu content was increased from 0 to 15 wt% over a 24 h period, and the selectivity towards 1,2-PD reached its maximum value of 97% at 2 h for 15wt% and 2 wt% Cu loadings. For 15 wt% Cu loaded on 25Ni–*y*Cu/AlO(OH), as the reaction proceeded for 24 h, the glycerol conversion reached its maximum at 89%, with a slight decline in selectivity to 79.3%, while the yield of 1,2-PD reached its peak at 70.6%. The 25Ni–15Cu/AlO(OH) catalyst exhibited the lowest average particle size distribution, small-pore characteristics, and high dispersion (Fig. 2(c), 3(d) and Table 1), leading to a larger number of active sites. Consequently, it is conceivable to achieve higher glycerol conversion and 1,2-PD selectivity. These observations confirm enhanced anti-oxidation and reducibility, indicative of a strong metal and support interaction and subsequently, a higher

density of active sites. This interaction is crucial in the hydrogenation of intermediate product, ultimately facilitating the synthesis of 1,2-PD.

Across the Ni- and Cu-loading catalyst series, the catalytic performance results clearly showed that activity and selectivity are governed by the combined metallic and acidic functions. Monometallic 10Cu/AlO(OH) exhibited very low glycerol conversion, consistent with the limited ability of Cu to activate H_2, even though Cu^0/Cu^+ sites are known to be effective for selective hydrogenation of C–O bonds.[56,64,65] In contrast, 25Ni/AlO(OH) achieved almost complete conversion but with poor selectivity of 1,2-PD, reflecting the strong, less selective hydrogenolysis behavior of Ni, which readily cleaves both C–O and, to some extent, the cleavage of C–C bonds. Introducing Cu into Ni to form bimetallic Ni–Cu/AlO(OH) catalysts significantly improves the balance between glycerol conversion and 1,2-PD selectivity. Across all Cu loadings (2–15 wt%), the catalysts exhibited substantially higher selectivity of 1,2-PD are obtained compared with the monometallic Ni and Cu counterparts, with 25Ni–10Cu and 25Ni–15Cu delivering the most favorable overall performance.

This behaviour can be rationalised by the structural and surface information obtained from characterisation results. Textural analysis confirmed that all catalysts remain mesoporous after the introduction of metal (Table 1), while XRD patterns and Vegard's law showed that reduction at 490 °C produces composition-tunable Ni–Cu alloys with nanoscale crystallites (5–8 nm) ranging from Cu-rich to Ni-rich phases (Fig. 2 and Table 2). XPS results (Fig. 6) indicated that the most active and selective catalysts formulations, 25Ni–10Cu and 25Ni–15Cu, combine comparatively high fractions of Ni^0 and Cu^0/Cu^+ with small positive shifts in both Ni $2p_{3/2}$ and Cu $2p_{3/2}$ binding energies, suggesting electronic interaction between Ni and Cu and partial alloy formation. Py-FTIR (Fig. 5) exhibited that all catalysts are dominated by Lewis acid sites, promoting glycerol dehydration to acetol, but variations in acidity alone cannot account for the observed 1,2-PD selectivity trends.

Altogether, these results support a cooperative mechanism in which Ni and Cu play synergistically roles for both hydrogenolysis activity and product selectivity. Cu^0/Cu^+ sites, in conjunction with Lewis acid sites on AlO(OH), facilitate the initial dehydration of glycerol to acetol, while Ni^0 sites serve as the primary centres for H_2 activation and subsequent hydrogenation of acetol to 1,2-PD.

In Cu-rich or intermediate alloys such as 25Ni–10Cu and 25Ni–15Cu, the electronic moderation of Ni by Cu, combined with the presence of nanoscale alloy domains, mitigates Ni's excessive hydrogenolysis strength and favours-controlled C–O bond cleavage over undesired C–C bond cleavage. Thus, the optimal Ni/Cu ratio not only increases the availability of active metal sites but also fine-tunes the alloy composition and surface oxidation states, thereby creating cooperative Ni–Cu ensembles that maximize glycerol conversion and 1,2-PD selectivity.[41,56,64,66]

3.2.3. Product distribution and reaction pathway. As the reaction time was extended from 2 to 24 h, there was a considerable increment in glycerol conversion but a subsequent reduction in selectivity and yield of 1,2-propanediol. Therefore, the optimal reaction time was determined to be 6 h, where a balance was achieved with high conversion, selectivity, and yield toward 1,2-PD. The component distributions for the catalysts were analyzed by GC-MS using total ion chromatograms (TIC) obtained at the optimal reaction time of 6 h and are presented in Table 3. The relative concentration of each component for the catalysts was calculated by the ratio of the specific peak area corresponding to a particular compound to the sum of all peak areas observed.

Table 3 Component distributions, determined by relative peak area in the TIC for AlO(OH) based catalysts analyzed by GC-MS at the optimal reaction time of 6 h

	Component distributions (%)			
Catalysts	Glycerol	1,2-PD	Acetol	EG
10Cu	81.8	17.2	0.8	0.2
25Ni	13.1	79.0	6.8	0.9
25Ni–10Cu	45.0	53.2	1.2	0.6
25Ni–15Cu	41.7	57.3	0.2	0.8

However, as indicated in the literature,[13] the application of noble metals such as Pt and Ru and some non-noble metal catalysts (Ni and Co) for the glycerol hydrogenolysis reaction, results in the production of low-molecular weight alcohols, including 1-propanol, methanol, and ethanol, as well as byproducts such as ethylene glycol (EG) *via* C–C bonds cleavage. In this work, as can be seen in Table 3, with the monometallic and bimetallic Ni–Cu catalysts over boehmite and/or other supports after 6 h reaction time, the main product is 1,2-PD.

Due to high selectivity of desired product obtained by this catalytic system, the potential of enhancing the catalyst performance to provide more economic benefits through lowering the cost of separation processes can greatly enhance the competitiveness in the 1,2-PD market.

The appearance of acetol in the GC-MS results confirms that the generation of 1,2-propanediol over these catalysts, under these operating conditions, proceeds through a two-step reaction mechanism, as indicated in Scheme 1. Glycerol is first transformed to acetol through a dehydration reaction on an acid catalyst. Then, the acetol is hydrogenated on a metal catalyst to produce 1,2-PD.[67–69] It seems that the incorporation of NiCu alloy over AlO(OH) in prepared catalysts exhibits a strong ability in the cleavage of C–O bonds while leaving limited the cleavage of C–C bonds.

Table 4 compares the catalytic performance of literature-reported NiCu-based systems and the Ni–Cu/AlO(OH) catalysts developed in this work. However, due to the varied reaction conditions and the use of different metal loadings and supports with different interactions reported in the literature, direct comparison of the results can be challenging.

NiCu-based catalysts, particularly those supported on alumina, consistently demonstrate high activity and selectivity toward 1,2-PD, benefiting from the synergistic interaction of Ni and Cu in promoting glycerol dehydration and the selective

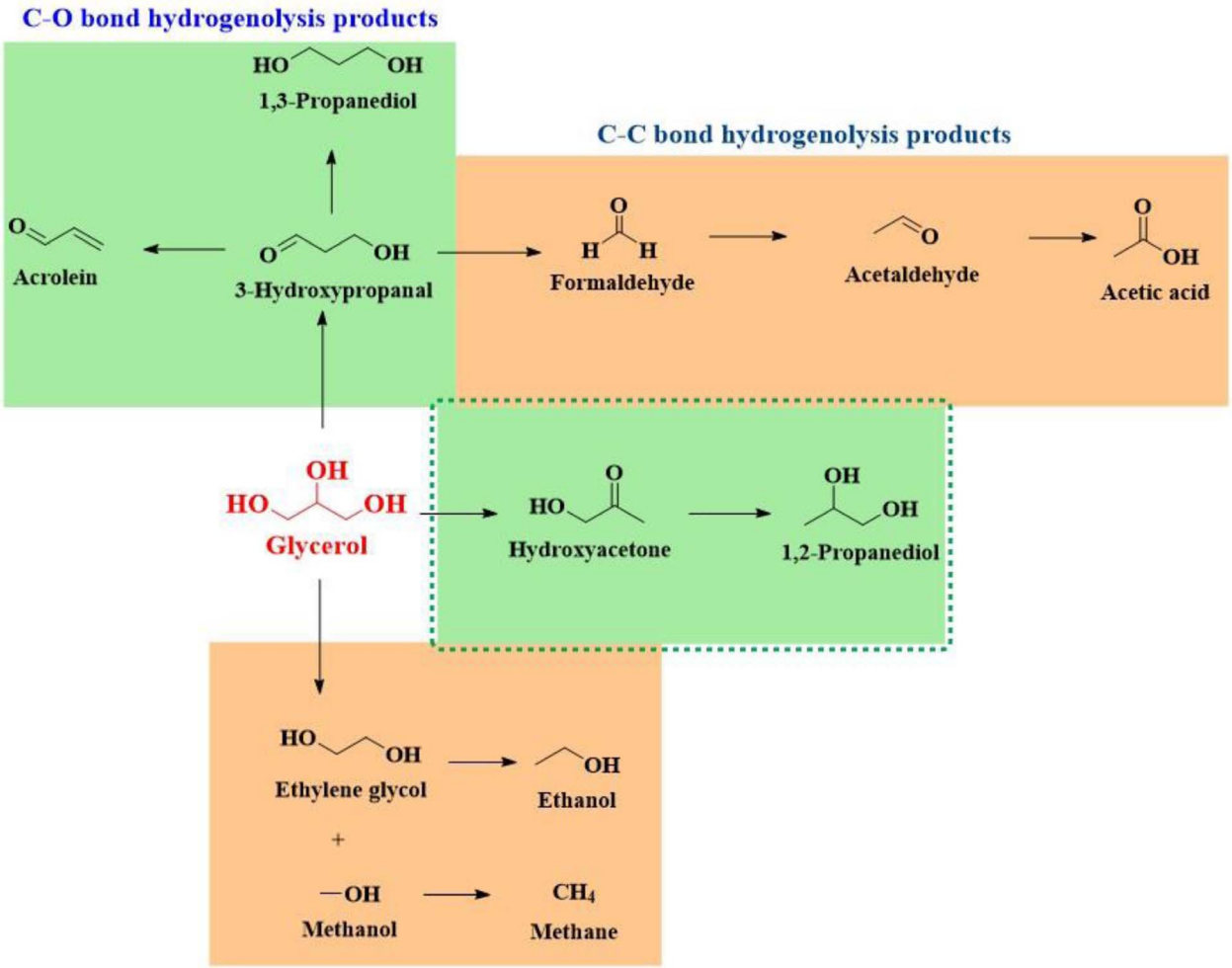

Scheme 1 Possible two-step glycerol hydrogenolysis reaction mechanism.[27]

hydrogenation pathways. In this study, the 25Ni–10Cu/AlO(OH) catalyst achieved a glycerol conversion of 90.2% and a 1,2-PD yield of 71.7% under 240 °C, 4 MPa H_2, and 24 h reaction time, demonstrating competitive performance with leading literature examples under comparable conditions. Similarly, the 25Ni–15Cu/AlO(OH) catalyst showed tunable selectivity, with short reaction times favoring high 1,2-PD selectivity (92.7%) and extended reaction times maximizing overall 1,2-PD yield of 70.6%. Furthermore, these results suggest that the catalytic activity of Ni–Cu/AlO(OH) systems could be further optimized by fine-tuning reaction conditions.

3.2.4. Operating condition optimization. To optimize the hydrogenolysis reaction parameters on the response functions (Y_1 = glycerol conversion and Y_2 = 1,2-PD yield), the Response Surface Methodology (RSM) was employed with a three-level, three independent variables in CCD to model the relationships between the response variables and the independent factors. A total of 20 experimental runs with different parameters were achieved, and the resulting experimental values are reported in Table 5. All experiments were performed in a randomized sequence at a 6 h reaction time and 20 wt% glycerol concentration. These factors were selected in the range of 200–240 °C, 350–750 psi, 2–6 wt%, respectively.

The results revealed a good agreement between the observed glycerol conversions and 1,2-PD yields and their predicted values. Model fitness was evaluated using the coefficient of determination (R^2) and the adjusted R^2 (Adj-R^2). A high R^2 value approaching unity and the closeness of the Adj-R^2 to the corresponding R^2 value indicate a more accurate model fit.[77] The analysis of p-values for glycerol conversion indicates the insignificance (p-value > 0.1) of interaction terms such as AC, ABC, AB^2, hydrogen pressure (B), and the square of hydrogen pressure (B^2). Consequently, these terms were eliminated from the model to enhance its accuracy. Similarly, in the case of 1,2-PD yield, the evaluation of p-values shows that the interaction of temperature, H_2 pressure, and catalyst loading (ABC), AB, A^2, B^2, and A^2B are not significant (p-value > 0.1), leading to their elimination from the model. The ANOVA tables for conversion and yield after the elimination of insignificant variables are reported in Tables 6 and 7, respectively.

After elimination of insignificant terms, the developed model achieved an R^2 value of 0.98 for glycerol conversion and 0.96 for 1,2-PD yield, indicating that 98.0% of the total variation

Table 4 Comparison of NiCu/AlO(OH) catalytic performance with literature

Catalysts	Conditions (T (°C), P (MPa), glycerol concentration (wt%), time (h))	Conversion (%)	1,2-PD selectivity (%)	1,2-PD yield (%)	Ref.
Ni–Cu/Al_2O_3(5%Ni, 62%Cu, 33%Al)	200, 4, 10, 24	67.1	90.1	60.4	24
Cu–Ni (1 : 1)/γ-Al_2O_3	210, 4.5, 20, 12	72.0	93.0	66.9	70
2.5Ru–2.5Cu/TiO_2	200, 2.5, 20, 12	53.9	95.0	51.2	71
Ni–Ce/AC	200, 5, 25, 6	90.4	65.7	59.4	72
Cu/boehmite	200, 4, 80, 6	77.5	92.5	83.8	73
$CuZnAl_2O_4$	180, 4, 80, 1	85.8	92.1	79.0	74
Ni–Cu/Al_2O_3	220, 4.5, 4, 24	70.5	67.0	47.2	61
9Cu–1Ni/mesoporous alumina (MA)	220, 4, 80, 24	76.6	55.3	42.4	62
$CuAl_2O_4$ spinel	220, 5, 100, 12	90.0	91.0	81.9	75
35%Cu/MgO	210, 4.5, 20, 12	96.6	92.6	89.5	76
25Ni–10Cu/TiO_2	240, 4, 20, 24	72.9	85.8	62.5	39
25Ni–10Cu/AlO(OH)	240, 4, 20, 4, 24	90.2	79.5	71.7	This work
25Ni–15Cu/AlO(OH)	240, 4, 20, 4, 6	65.1	92.7	60.3	This work
25Ni–15Cu/AlO(OH)	240, 4, 20, 4, 24	89.0	79.3	70.6	This work

in glycerol conversion and 96.2% in 1,2-PD yield could be explained by the investigated experimental parameters. Furthermore, the close proximity of the Adj-R^2 value (0.97 for conversion and 0.94 for yield) to the R^2 value confirms the adequacy of the models, presented (Table 8).

Adequate precision was alternatively employed as an appropriate statistical model precession for determining the signal-to-noise ratio, with a preference for a value surpassing 4.[78,79] As presented in Table 6, adequate precision was determined to be 31.64 for glycerol conversion and 22.41 for 1,2-PD yield, confirming the statistical significance of the models. Moreover, the coefficients of variation (C. V.) for the Y_1 and Y_2 models were 5.04% and 3.94%, respectively, with a preferred value of less than 10%.[79] This indicates a justifiable correlation between the actual and predicted values.

The impact of independent variables on the hydrogenolysis of glycerol on the values of glycerol conversion and 1,2-PD yield (response functions) was provided in terms of coded factors, expressed in eqn (5) and (6), respectively:

$$\mathrm{Sqrt}(Y_1) = 5.81 + 0.80A + 0.97C - 0.75AB - 0.38BC + 1.32A^2 - 2.49C^2 + 0.55A^2B - 1.41A^2C \quad (5)$$

$$\mathrm{Sqrt}(Y_2 + 25) = 7.26 + 1.91A + 0.29B + 0.63C - 0.35AC + 0.21BC - 1.18C^2 - 0.88A^2C - 1.44AB^2 \quad (6)$$

Table 5 CCD matrix and the value of response functions at a 6 h reaction time and 20 wt% glycerol concentration

Run	A: temperature (°C)	B: pressure (psi)	C: catalyst loading (wt%)	Y_1: conversion (%)	Predicted conversion (%)	Y_2: yield (%)	Predicted yield (%)
1	200.0	350.0	2.0	7.8	6.8	7.4	4.0
2	240.0	350.0	2.0	30.6	32.0	24.4	24.9
3	200.0	750.0	2.0	36.6	35.3	4.4	6.5
4	240.0	750.0	2.0	35.7	36.2	29.3	27.5
5	200.0	350.0	6.0	5.9	6.2	4.1	1.8
6	240.0	350.0	6.0	32.0	30.7	5.1	4.7
7	200.0	750.0	6.0	18.9	18.7	12.6	13.9
8	240.0	750.0	6.0	19.6	19.3	17.2	16.6
9	200.0	550.0	4.0	36.2	39.4	4.4	3.2
10	240.0	550.0	4.0	65.0	61.6	60.3	55.3
11	220.0	350.0	4.0	27.9	33.6	14.9	23.9
12	220.0	750.0	4.0	30.2	33.6	29.8	31.8
13	220.0	550.0	2.0	5.1	5.7	2.7	4.9
14	220.0	550.0	6.0	17.7	18.7	17.6	19.9
15	220.0	550.0	4.0	35.7	33.6	29.3	27.9
16	220.0	550.0	4.0	35.7	33.6	29.3	27.9
17	220.0	550.0	4.0	35.7	33.6	29.3	27.9
18	220.0	550.0	4.0	35.7	33.6	29.3	27.9
19	220.0	550.0	4.0	35.7	33.6	29.3	27.9
20	220.0	550.0	4.0	35.7	33.6	29.3	27.9

Table 6 .ANOVA table for the conversion of glycerol after elimination of insignificant terms

	Sum of squares	df	Mean square	*F* value	*p*-value	
Model	37.88	8	4.74	68.41	<0.0001	Significant
A-Temperature	6.43	1	6.43	92.93	<0.0001	
C-Catalyst loading	1.90	1	1.90	27.43	0.0003	
AB	4.44	1	4.44	64.18	<0.0001	
BC	1.13	1	1.13	16.38	0.0019	
A^2	5.54	1	5.54	80.01	<0.0001	
C^2	19.88	1	19.88	287.25	<0.0001	
A^2B	2.41	1	2.41	34.78	<0.0001	
A^2C	3.18	1	3.18	45.99	<0.0001	
Residual	0.76	11	0.07			
Lack of fit	0.76	6	0.13			
Pure error	0.00	5	0.00			
Cor total	38.64	19				

To maximize the response, the response surface plots of glycerol conversion and 1,2-PD yield, derived from the mathematical models, provided insights into the interactive impacts of temperature, pressure, and catalyst loading on the hydrogenolysis process for 1,2-PD production. Fig. 9(a)–(d) shows the effects of all three operating conditions, which remained consistent with the data obtained in the experiments, on glycerol conversion and 1,2-PD yield.

In the mutual interaction of reaction temperature and hydrogen pressure on glycerol conversion depicted in Fig. 9(a), reaction temperature has a significant impact on the conversion of glycerol. Notably, increasing the temperature progressively from 200 to 240 °C correlates positively with enhanced glycerol conversion rates. The favorable impact of reaction temperature on glycerol conversion may be attributed to enhance reaction kinetics, facilitating the cleavage of C–C and C–O bonds, and reducing the viscosity of the reaction mixture at higher temperatures.[2] In the meantime, as the pressure increased from 350 to 750 psi, there is a marginal uptick observed in the conversion rates of glycerol. The maximum conversion rate was achieved at 240 °C and 550 psi, with subsequent notable conversion (37%) occurring at 750 psi, 200 °C, and 2 wt% catalyst loading. It can be attributed to the increasing solubility of hydrogen molecules in the liquid media, which then enhances the hydrogenolysis of glycerol with increasing pressure.[9]

Table 8 Statistical parameters of the designed models

	Value	
Summary statistics	Y_1	Y_2
Std. dev.	0.26	0.26
Mean	5.22	6.67
C. V.%	5.04	3.94
R^2	0.98	0.96
Adjusted R^2	0.97	0.94
Predicted R^2	0.94	0.85
Adeq. precision	31.64	22.41
Press	2.47	3.07

Based on the response surface model shown in Fig. 9(b), it is evident that the interaction between hydrogen pressure and catalyst loading significantly influenced the conversion of glycerol. Specifically, at a H_2 pressure of approximately 550 psi and a catalyst loading of 4 wt%, the highest glycerol conversion of 65% is achieved. Further analysis indicated that increasing the catalyst loading up to 4 wt% enhances glycerol conversion; however, surpassing this threshold results in a decline in

Table 7 ANOVA table for the yield of 1,2-propanediol after elimination of insignificant terms

	Sum of squares	df	Mean square	*F* value	*p*-value	
Model	19.45	8	2.43	35.24	<0.0001	Significant
A-Temperature	7.27	1	7.27	105.40	<0.0001	
B-Pressure	0.84	1	0.84	12.22	0.0050	
C-Catalyst loading	0.80	1	0.80	11.57	0.0059	
AC	1.00	1	1.00	14.48	0.0029	
BC	0.35	1	0.35	5.09	0.0453	
C^2	6.94	1	6.94	100.57	<0.0001	
A^2C	1.25	1	1.25	18.05	0.0014	
AB^2	3.32	1	3.32	48.05	<0.0001	
Residual	0.76	11	0.07			
Lack of fit	0.76	6	0.13			
Pure error	0.00	5	0.00			
Cor total	20.21	19				

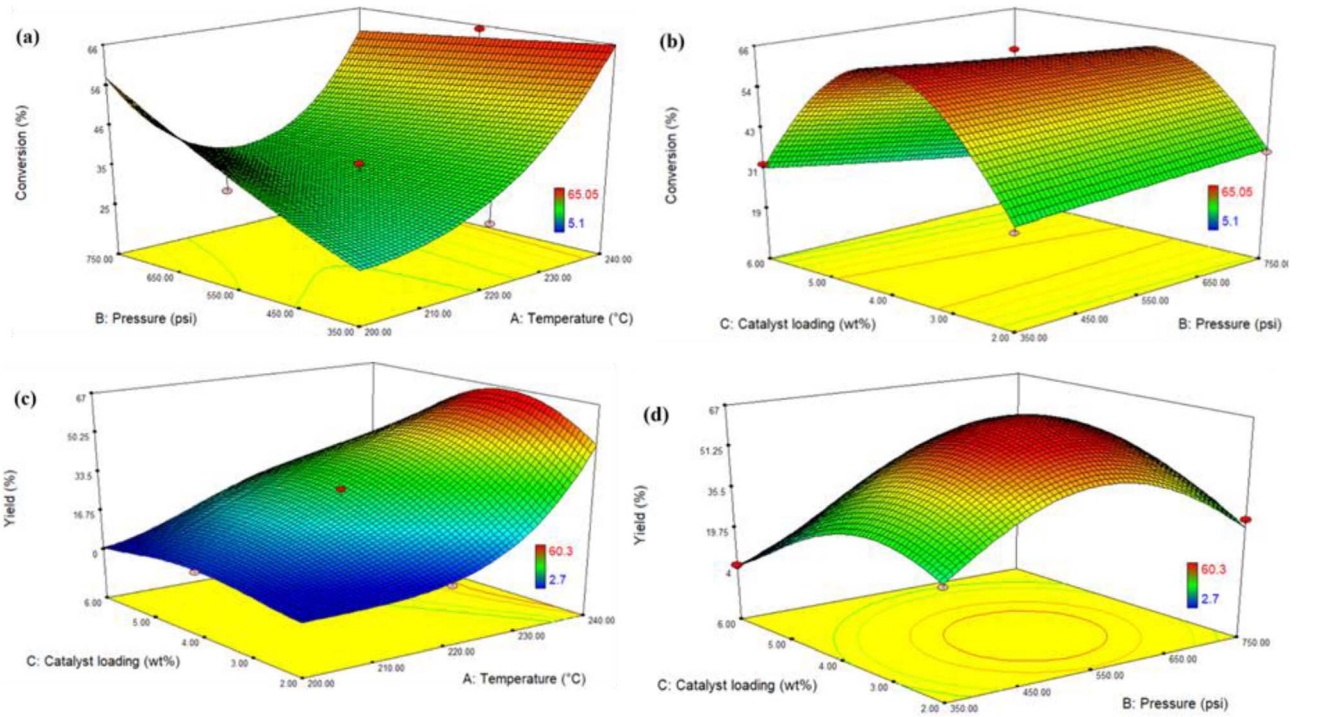

Fig. 9 Effects of the independent variables studied on glycerol conversion (a and b) and 1,2-PD yield (c and d) at optimized condition of 240 °C, 515 psi, and 4.10 wt%.

conversion efficiency. The increase in conversion with a higher catalyst quantity is attributed to the enhanced accessibility of the active catalyst surface with the glycerol solution. However, to balance economic considerations and the limited solubility of the catalyst, it is preferable to introduce a moderate quantity of catalyst. A higher concentration of catalyst could exacerbate the occurrence of undesirable side reactions.[80] Meanwhile, the glycerol conversion was nearly plateauing as the H_2 pressure increased, suggesting that the H_2 pressure was not a major contributor. The ANOVA table, which indicated that H_2 pressure had a higher *p*-value of 0.5909, further supported this conclusion. Fig. 9(c) illustrates the combined influence of reaction temperature (ranging 200 to 240 °C) and catalyst loading (ranging 2 to 6 wt%) at a constant hydrogen pressure of 550 psi on the yield of 1,2-propanediol. There is a more notable effect on the yield of 1,2-PD upon variation in temperature as compared to catalyst loading. By increasing the reaction temperature from 200 to 240 °C at the catalyst loading of 4 wt%, the yield of 1,2-PD was increased from almost 4.4% (12.1% 1,2-PD selectivity) to the highest yield of 60.3% (92.7% 1,2-PD selectivity). The 1,2-PD yield significantly increases from 2.7 to 60.3% with enhancement in temperature from 200 °C to 240 °C at the catalyst loading between 2 and 4 wt%. These results also indicate that a high active surface area, achieved by increasing the catalyst loading from 2 to 4 wt%, promotes the selective transformation of glycerol into 1,2-PD through the dehydration–hydrogenation pathway, while suppressing the side reactions that form degradation products.

The 3-D surface plots for the two independent variables, pressure and catalyst loading, as shown in Fig. 9(d), exhibited a saddle-like shape, suggesting the existence of an optimal value for the yield of 1,2-propanediol between these two variables. It can be observed that there is a positive correlation between 1,2-PD yield and the increase of pressure or catalyst loading. The 1,2-PD yield reached a maximum value of 60.3% (92.7% 1,2-PD selectivity) at the H_2 pressure of 550 psi and 4 wt% catalyst loading and exhibited a subsequent decline with the increase of pressure or catalyst loading. It could be reasoned that increasing hydrogen pressure enhanced the diffusion mass transfer of hydrogen, promoting the transport of hydrogen molecules into the internal catalyst channels where they can dissociate on Ni–Cu and react with glycerol and water (reactants) on the catalyst surface. However, very high pressure can also easily cause cracking reactions.[81] Moreover, there is not a significant impact between pressure and temperature, as also shown in ANOVA table as an insignificant factor.

The response surface models developed showed that the optimal conditions for maximizing the glycerol conversion and 1,2-propanediol yield were determined to be a temperature of 240 °C, a pressure of 550 psi, and a catalyst loading of 4 wt%, resulting in 63% glycerol conversion and 59% yield of 1,2-PD. These optimal reaction conditions were validated experimentally, and the results confirmed the predictive capability of the developed model within experimental constraints.

3.2.5. Reusability test of 25Ni–15Cu/AlO(OH). The effective catalyst recyclability and reuse are critical for optimizing chemical reactions, enhancing sustainability in industrial processes, and advancing green chemistry principles.[82] The reusability of 25Ni–15Cu/AlO(OH) for the hydrogenolysis of glycerol under optimized conditions (240 °C, 550 psi, 4 wt%

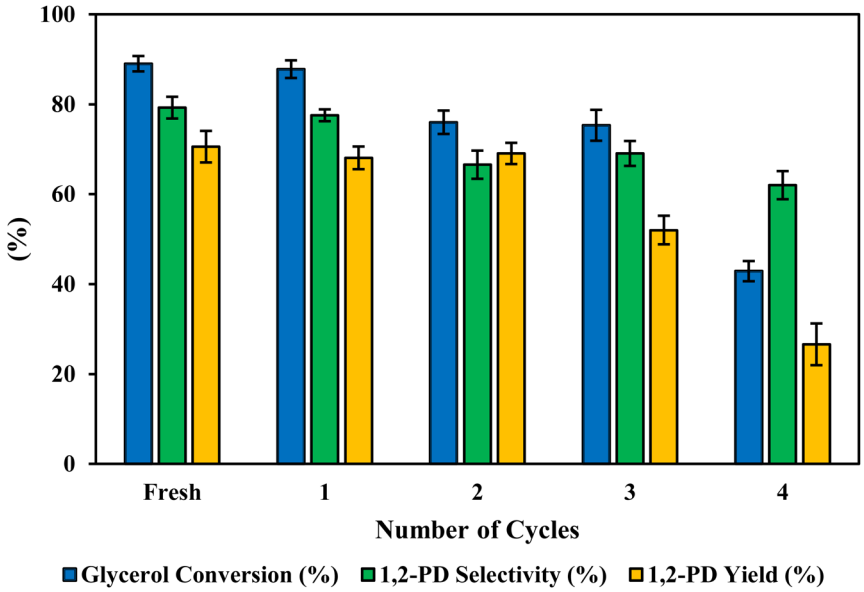

Fig. 10 Reusability of 25Ni–15Cu/AlO(OH) for hydrogenolysis of glycerol to 1,2-PD at optimized condition of 240 °C, 550 psi, and 4 wt% after 24 h reaction time.

catalyst loading) for 24 h over four consecutive cycles is presented in Fig. 10. In the fresh run, the catalyst achieved approximately 89% glycerol conversion, 79.3% 1,2-PD selectivity, and 70.6% yield. However, a progressive decline in performance was observed across cycles. A sharp deactivation occurred in cycle 4, with glycerol conversion falling to ~43%, 1,2-PD selectivity to ~62%, and yield to ~27%. This trend indicates the catalyst remains moderately stable for the first three cycles, followed by significant loss of activity, likely from deactivation effects.

TGA (Fig. 11(a)) showed a progressive decrease in weight loss from 14.1% for the fresh catalyst to 7.7% in cycle 4. In all cases, the low-temperature weight loss is attributed to removal of physisorbed water and surface hydroxyl groups, while the higher-temperature region (200–500 °C) is associated with dehydroxylation of boehmite-derived alumina and combustion of residual organic species.[83,84]

The progressive reduction in total weight loss over successive reaction cycles suggests the absence of extensive coke deposition. Instead, it reflects the irreversible elimination of a fraction of labile surface hydroxyl groups during the initial run, leading to a more dehydroxylated surface that exhibits a lower subsequent weight loss on heating. Thus, carbonaceous deposits make only a minor contribution to the observed loss in activity, and coking can be excluded as the primary deactivation mechanism.

The XRD analysis (Fig. 11(b)) shows that after four cycles, the spent catalyst preserves the phase pattern of the *ex situ* reduced catalyst sample. The reflections are slightly more intense and marginally broadened in spent catalyst, suggesting modest crystallite growth or partial surface oxidation rather than the phase transformation, and bulk sintering or support collapse are limited. This preserved bulk structure is consistent with the relatively stable selectivity observed in the early cycles. Moreover, no evidence of carbonaceous species, such as coke at $2\theta \approx 26°$, implying that catalyst deactivation *via* coking is not a major deactivation pathway.[85]

In contrast, XPS analysis of the fourth cycled catalyst reveals increased near-surface oxidation and lower metallic peak intensity relative to the fresh *ex situ* reduced catalyst sample, indicating partial surface re-oxidation and a reduced accessible metal surface area after, as shown in Fig. 11(c) and (d). Moreover, the overall Ni $2p_{3/2}$ and Cu $2p_{3/2}$ signal intensities are clearly lower for the spent catalyst than for the fresh reduced sample. These observations indicate that repeated operation under hot aqueous conditions leads to progressive surface oxidation of Ni and Cu and to a loss or burial of metal at the outer surface, for example through migration into Ni–Al–O and Cu–Al–O environments or partial leaching of metal into the liquid phase during prolonged operation.[47,86] Although metal leaching was not quantified here, such behaviour is commonly reported for Ni–Cu catalysts in hot aqueous media and is consistent with the reduced Ni and Cu XPS signals after reaction cycling. Cai *et al.*[66] reported that the Ni–Cu catalysts exhibited more deactivation during aqueous-phase glycerol hydrogenolysis, primarily associated with metal particle sintering and metal leaching processes. As metallic Ni^0 provides sites for H_2 activation and C–O bond hydrogenolysis, and Cu^0/Cu^+ promotes glycerol dehydration and stabilization of oxygenated intermediates, the combined decrease in metallic Ni and Cu fractions, the lower surface concentration of Ni and Cu, and the moderate sintering of Ni–Cu particles, collectively diminishes the number of active Ni–Cu ensembles accessible for the glycerol hydrogenolysis pathway. This explains the gradual drop in glycerol conversion, while the remaining alloyed Ni–Cu sites still favour the formation of 1,2-PD, thereby maintaining

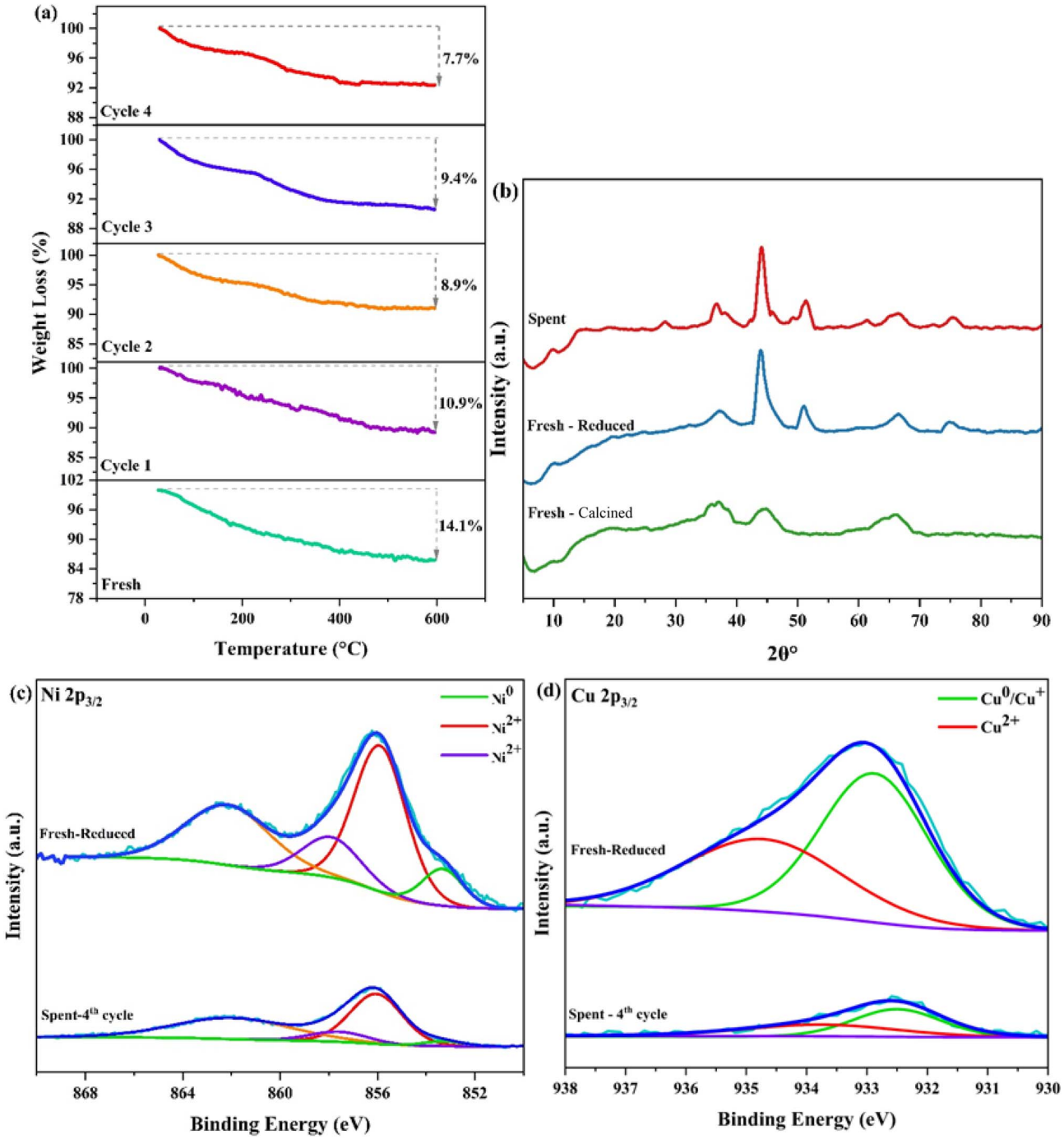

Fig. 11 (a) TGA profiles of the fresh 25Ni–15Cu/AlO(OH) catalyst and after each reaction cycle; (b) XRD patterns of 25Ni–15Cu/AlO(OH) for the fresh calcined, fresh *ex situ* reduced, and spent catalyst after cycle 4; (c and d) Ni $2p_{3/2}$ and Cu $2p_{3/2}$ XPS spectra of fresh *ex situ* reduced and spent 25Ni–15Cu/AlO(OH) after cycle 4.

relatively high selectivity. Overall, the reusability tests and post-reaction characterization indicate that deactivation of 25Ni–15Cu/AlO(OH) is primarily governed by progressive surface oxidation and partial loss or redistribution of Ni and Cu species, with mild sintering and support dehydroxylation playing secondary roles, rather than by extensive coke deposition or bulk structural degradation.

4. Conclusions

The influence of different NiCu loadings over AlO(OH) for the liquid phase hydrogenolysis of glycerol to 1,2-propanediol was investigated to determine the optimal NiCu/AlO(OH) formulation that maximizes 1,2-PD yield while minimizing undesirable by-products. The characterization of the NiCu/AlO(OH) catalysts prepared *via* the impregnation method indicated several

notable features: a large specific surface area, insignificant agglomeration, an abundance of active sites for hydrogenolysis, the formation of favorable electronic interface between the Ni and Cu alloy, and optimal Lewis acid sites that enhance the dehydration of glycerol to acetol. In the investigation of the impact of NiCu loadings on AlO(OH), a constant Cu loading of 10 wt% was maintained while Ni loadings varied from 0 to 30 wt%. The catalyst with 25 wt% Ni loading (25Ni–10Cu/AlO(OH)) presented the highest yield of 1,2-PD at 71.7%, with 79.5% selectivity for 1,2-PD and 90.2% glycerol conversion for 24 h of reaction time. Subsequently, varying the Cu loading from 2 to 15 wt% as a co-catalyst demonstrated that the highest selectivity for 1,2-PD was achieved with 15 wt% Cu incorporated into the 25 wt% Ni/AlO(OH) catalyst, achieving a selectivity of 92.7% and a 1,2-PD yield of 60.3% for 6 h of reaction time. These results highlight the significant impact of Cu in enhancing 1,2-PD selectivity. Subsequently, the optimization of operating conditions (temperature, H_2 pressure, and catalyst loading) for 25Ni–15Cu/AlO(OH) as a representative catalyst, at a 20 wt% glycerol concentration and a 6 h reaction time using CCD, led to the optimal glycerol conversion and 1,2-PD yield. These findings show that the maximum conversion of 62%, with 53.35% 1,2-PD yield (86.0% 1,2-PD selectivity), can be achieved under optimal reaction parameters of 240 °C, 515 psi, and 4.1 wt% catalyst loading, consistent with experimental results. The high selectivity of 1,2-PD achieved in a shorter reaction duration (6 h) using the 25Ni–15Cu/AlO(OH) catalyst, consisting of economically feasible metals and utilizing a two-step reaction mechanism with minimal production of undesired products.

Reusability tests further indicate moderate stability over the first 3 cycles, with the later conversion loss governed primarily by partial surface re-oxidation and mild sintering, rather than coking, highlighting the need to preserve Ni–Cu alloy interfaces during regeneration.

Author contributions

Asma Ghorbani: conceptualization, data curation, formal analysis, investigation, methodology, validation, visualization, writing – original draft, writing – review & editing. Ajay Dalai: conceptualization, funding acquisition, project administration, writing – review & editing, supervision.

Conflicts of interest

The authors declare that no conflicts, personal or financial, appear to influence this work.

Data availability

Data for this article, including catalyst characterization data and experimental results, are available at Zendo at https://doi.org/10.5281/zenodo.17971348.

Supplementary information (SI): detailing the distribution of acid sites and XPS binding energies. See DOI: https://doi.org/10.1039/d5ra07593a.

Acknowledgements

The authors acknowledge the funding from Canada Research Chair (CRC) Program and Natural Sciences, Engineering Research Council of Canada (NSERC), and Agriculture Development Funds (ADF) for this research. The authors are also thankful to the Saskatchewan Structural Sciences Center (SSSC) at the University of Saskatchewan for assisting with XPS and XRD Characterizations. The authors extend their sincere appreciation to Dr Venu Borugadda, Post Doctoral Fellows at the University of Saskatchewan, for his valuable guidance.

References

1 I. C. Freitas, R. L. Manfro and M. M. V. M. Souza, *Appl. Catal., B*, 2018, **220**, 31–41, DOI: 10.1016/j.apcatb.2017.08.030.
2 T. Numpilai, C. K. Cheng, A. Seubsai, K. Faungnawakij, J. Limtrakul and T. Witoon, *Environ. Pollut.*, 2021, **272**, 116029, DOI: 10.1016/j.envpol.2020.116029.
3 A. Kostyniuk, D. Bajec, P. Djinović and B. Likozar, *Chem. Eng. J.*, 2020, **397**, 125430, DOI: 10.1016/j.cej.2020.125430.
4 S. S. Priya, V. P. Kumar, M. L. Kantam, S. K. Bhargava, A. Srikanth and K. V. R. Chary, *Ind. Eng. Chem. Res.*, 2015, **54**, 9104–9115, DOI: 10.1021/acs.iecr.5b01814.
5 S. Bhowmik and S. Darbha, *Catal. Rev.*, 2021, **63**, 639–703, DOI: 10.1080/01614940.2020.1794737.
6 S. P. Samudrala, *Glycerine Production and Transformation—An Innovative Platform for Sustainable Biorefinery and Energy*, 2019.
7 A. Ghorbani, V. B. Borugadda and A. K. Dalai, *Renewable Sustainable Energy Rev.*, 2025, **224**, 116054, DOI: 10.1016/j.rser.2025.116054.
8 S. Zhu, X. Gao, Y. Zhu and Y. Li, *J. Mol. Catal. A: Chem.*, 2015, **398**, 391–398, DOI: 10.1016/j.molcata.2014.12.021.
9 S. Chanklang, W. Mondach, P. Somchuea, T. Witoon, M. Chareonpanich, K. Faungnawakij and A. Seubsai, *Catal. Today*, 2022, **397–399**, 356–364, DOI: 10.1016/j.cattod.2021.08.014.
10 V. Korpelin, G. Sahoo, R. Ikonen and K. Honkala, *J. Catal.*, 2023, **422**, 12–23, DOI: 10.1016/j.jcat.2023.03.032.
11 A. D. da Silva Ruy, R. M. de Brito Alves, T. L. R. Hewer, D. de Aguiar Pontes, L. S. G. Teixeira and L. A. M. Pontes, *Catal. Today*, 2021, **381**, 243–253, DOI: 10.1016/j.cattod.2020.06.035.
12 D. Sun, Y. Yamada, S. Sato and W. Ueda, *Appl. Catal., B*, 2016, **193**, 75–92, DOI: 10.1016/j.apcatb.2016.04.013.
13 D. K. Pandey and P. Biswas, *Energy Fuels*, 2023, **37**(10), 6879–6906, DOI: 10.1021/acs.energyfuels.2c03806.
14 R. Mane, Y. Jeon and C. Rode, *Green Chem.*, 2022, **24**, 6751–6781, DOI: 10.1039/d2gc01879a.
15 S. N. Delgado, L. Vivier and C. Especel, *Catal. Commun.*, 2014, **43**, 107–111, DOI: 10.1016/j.catcom.2013.09.021.
16 H. Mitta, P. K. Seelam, S. Ojala, R. L. Keiski and P. Balla, *Appl. Catal., A*, 2018, **550**, 308–319, DOI: 10.1016/j.apcata.2017.10.019.
17 S. Zhu, X. Gao, Y. Zhu, Y. Zhu, H. Zheng and Y. Li, *J. Catal.*, 2013, **303**, 70–79, DOI: 10.1016/j.jcat.2013.03.018.

18 C. H. Zhou, K. Deng, M. Di Serio, S. Xiao, D. S. Tong, L. Li, C. X. Lin, J. Beltramini, H. Zhang and W. H. Yu, *Mol. Catal.*, 2017, **432**, 274–284, DOI: 10.1016/j.mcat.2017.02.008.
19 N. K. Mishra, P. Kumar, V. C. Srivastava and U. L. Stangar, *J. Environ. Chem. Eng.*, 2021, **9**(4), 105263, DOI: 10.1016/j.jece.2021.105263.
20 T. S. de Andrade, M. M. V. M. Souza and R. L. Manfro, *Renew. Energy*, 2020, **160**, 919–930, DOI: 10.1016/j.renene.2020.06.060.
21 H. Zhao, L. Zheng, X. Li, P. Chen and Z. Hou, *Catal. Today*, 2020, **355**, 84–95, DOI: 10.1016/j.cattod.2019.03.011.
22 M. H. M. Pires, F. B. Passos and Y. Xing, *Catal. Today*, 2023, **419**, 114161, DOI: 10.1016/j.cattod.2023.114161.
23 E. S. Vasiliadou and A. A. Lemonidou, *Chem. Eng. J.*, 2013, **231**, 103–112, DOI: 10.1016/j.cej.2013.06.096.
24 M. K. Poddar, A. Pandey, M. K. Jha, S. C. Andola, S. S. Ali, S. Bhandari, G. K. Sahani and R. Bal, *Mol. Catal.*, 2021, **515**, 111943, DOI: 10.1016/j.mcat.2021.111943.
25 F. Vila, M. López Granados, M. Ojeda, J. L. G. Fierro and R. Mariscal, *Catal. Today*, 2012, **187**, 122–128, DOI: 10.1016/j.cattod.2011.10.037.
26 J. Huang, J. Zhang, S. Lu, Y. Liang and F. S. Xiao, *Biomass Bioenergy*, 2023, **174**, 106818, DOI: 10.1016/j.biombioe.2023.106818.
27 A. Ghorbani, P. Boahene and A. K. Dalai, *Sustain. Energy Fuels*, 2025, **9**, 5657–5672, DOI: 10.1039/D5SE00480B.
28 S. S. Priya, P. Bhanuchander, V. P. Kumar, D. K. Dumbre, S. R. Periasamy, S. K. Bhargava, M. Lakshmi Kantam and K. V. R. Chary, *ACS Sustain. Chem. Eng.*, 2016, **4**, 1212–1222, DOI: 10.1021/acssuschemeng.5b01272.
29 W. F. Xu, P. Y. Niu, H. Q. Guo, L. T. Jia and D. B. Li, *J. Fuel Chem. Technol.*, 2021, **49**(9), 1270–1280, DOI: 10.1016/S1872-5813(21)60101-9.
30 A. A. Greish, E. D. Finashina, O. P. Tkachenko and L. M. Kustov, *Molecules*, 2021, **26**(6), 1565, DOI: 10.3390/molecules26061565.
31 A. J. Van Dillen, R. J. A. M. Terörde, D. J. Lensveld, J. W. Geus and K. P. De Jong, *J. Catal.*, 2003, **216**(1–2), 257–264, DOI: 10.1016/S0021-9517(02)00130-6.
32 P. Munnik, P. E. De Jongh and K. P. De, *Jong*, 2015, **115**(14), 6687–6718, DOI: 10.1021/cr500486u.
33 J. F. Zeitoune, C. D. M. Nickel, B. L. D. Santos, W. A. A. Macedo, D. A. Duarte and R. C. Catapan, *Energy Fuels*, 2024, **38**, 22471–22481, DOI: 10.1021/acs.energyfuels.4c04113.
34 J. Feng, Y. Zhang, W. Xiong, H. Ding and B. He, *Catalysts*, 2016, **6**(4), 51, DOI: 10.3390/catal6040051.
35 H. Liu, Z. Huang, H. Kang, X. Li, C. Xia, J. Chen and H. Liu, *Appl. Catal., B*, 2018, **220**, 251–263, DOI: 10.1016/j.apcatb.2017.08.022.
36 V. G. S. Mendonça, I. C. Freitas, R. L. Manfro and M. M. V. M. Souza, *Appl. Catal., A*, 2022, **645**, 118838, DOI: 10.1016/j.apcata.2022.118838.
37 Y. Sheng, X. Lin, S. Yue, Y. Liu, X. Zou, X. Wang and X. Lu, *Mater. Adv.*, 2021, **2**(20), 6722–6730, DOI: 10.1039/d1ma00557j.
38 D. Li, M. Lu, K. Aragaki, M. Koike, Y. Nakagawa and K. Tomishige, *Appl. Catal., B*, 2016, **192**, 171–181, DOI: 10.1016/j.apcatb.2016.03.052.
39 A. Ghorbani and A. K. Dalai, *Can. J. Chem.*, 2025, **103**(6), 280–292, DOI: 10.1139/cjc-2024-0265.
40 J. Liu, Y. Zheng and S. Hou, *RSC Adv.*, 2017, **7**(60), 37823–37829, DOI: 10.1039/c7ra06062a.
41 B. C. Miranda, R. J. Chimentão, J. Szanyi, A. H. Braga, J. B. O. Santos, F. Gispert-Guirado, J. Llorca and F. Medina, *Appl. Catal., B*, 2015, **166**, 166–180, DOI: 10.1016/j.apcatb.2014.11.019.
42 M. Mohammadi, M. Khodamorady, B. Tahmasbi, K. Bahrami and A. Ghorbani-Choghamarani, *J. Ind. Eng. Chem.*, 2021, **97**, 1–78, DOI: 10.1016/j.jiec.2021.02.001.
43 L. Zheng, Z. Li, P. Fu, F. Sun, M. Liu, T. Guo and Q. Fan, *ACS Omega*, 2022, **7**(31), 27172–27184, DOI: 10.1021/acsomega.2c01742.
44 C. Lv, L. Xu, M. Chen, Y. Cui, X. Wen, Y. Li, C. E. Wu, B. Yang, Z. Miao, X. Hu and Q. Shou, *Front. Chem.*, 2020, **8**, 269, DOI: 10.3389/fchem.2020.00269.
45 H. Kweon, S. Jang, A. Bereketova, J. Chan Park and K. H. Park, *RSC Adv.*, 2019, **9**(25), 14154–14159, DOI: 10.1039/c9ra01608b.
46 A. Gil, *Catal. Today*, 2023, **423**, 114016, DOI: 10.1016/j.cattod.2023.01.023.
47 B. C. Vance, S. Najmi, P. A. Kots, C. Wang, S. Jeon, E. A. Stach, D. N. Zakharov, N. Marinkovic, S. N. Ehrlich, L. Ma and D. G. Vlachos, *JACS Au*, 2023, **3**(8), 2156–2165, DOI: 10.1021/jacsau.3c00232.
48 F. Zhao, M. Gong, Y. Zhang and J. Li, *J. Porous Mater.*, 2016, **23**(3), 733–740, DOI: 10.1007/s10934-016-0128-9.
49 Z. Shi, Q. Zhang, G. Yang, L. Liu, G. Wang, R. Ekananda, I. Gamar, R. Wang and R. Zhuo, *RSC Adv.*, 2025, **15**, 7563–7570, DOI: 10.1039/D5RA00527B.
50 T. Zhu, H. Song, F. Li and Y. Chen, *Catalysts*, 2020, **10**(3), 274, DOI: 10.3390/catal10030274.
51 N. Sudheer, V. Rouchon, D. Ihiawakrim, C. Lefebvre, P. Levitz, E. Lecolier, P. Rabu and O. Ersen, *Sci. Technol. Energy Transition*, 2024, **79**, 84, DOI: 10.2516/stet/2024050.
52 W. Lueangchaichaweng, B. Singh, D. Mandelli, W. A. Carvalho, S. Fiorilli and P. P. Pescarmona, *Appl. Catal., A*, 2019, **571**, 180–187, DOI: 10.1016/j.apcata.2018.12.017.
53 W. Xu, P. Niu, H. Guo, L. Jia and D. Li, *React. Kinet., Mech. Catal.*, 2021, **133**(1), 173–189, DOI: 10.1007/s11144-021-01988-9.
54 C. Miao, G. Zhou, S. Chen, H. Xie and X. Zhang, *Renew. Energy*, 2020, **153**, 1439–1454, DOI: 10.1016/j.renene.2020.02.099.
55 M. Kalong, P. Hongmanorom, S. Ratchahat, W. Koo-amornpattana, K. Faungnawakij, S. Assabumrungrat, A. Srifa and S. Kawi, *Fuel Process. Technol.*, 2021, **214**, 106721, DOI: 10.1016/j.fuproc.2020.106721.
56 W. Fang, S. Liu, A. K. Steffensen, L. Schill, G. Kastlunger and A. Riisager, *ACS Catal.*, 2023, **13**(13), 8437–8444, DOI: 10.1021/acscatal.3c01767.

57 J. Li, L. Shi, G. Feng, Z. Shi, C. Sun and D. Kong, *Catalysts*, 2020, **10**(10), 1215, DOI: 10.3390/catal10101215.
58 L. Sun, W. Luo, W. Sun and J. Yang, *Res. Chem. Intermed.*, 2019, **45**, 2903–2913, DOI: 10.1007/s11164-019-03769-5.
59 B. Seemala, C. M. Cai, C. E. Wyman and P. Christopher, *ACS Catal.*, 2017, **7**(6), 4070–4082, DOI: 10.1021/acscatal.7b01095.
60 Y. Song, S. Weng, F. Xue, A. J. McCue, L. Zheng, Y. He, J. Feng, Y. Liu and D. Li, *ACS Catal.*, 2023, **13**, 1952–1963, DOI: 10.1021/acscatal.2c06091.
61 I. Gandarias, P. L. Arias, J. Requies, M. El Doukkali and M. B. Güemez, *J. Catal.*, 2011, **282**(1), 237–247, DOI: 10.1016/j.jcat.2011.06.020.
62 Y. S. Yun, D. S. Park and J. Yi, *Catal. Sci. Technol.*, 2014, **4**(9), 3191–3202, DOI: 10.1039/c4cy00320a.
63 S. Zhu, X. Gao, Y. Zhu, J. Cui, H. Zheng and Y. Li, *Appl. Catal., B*, 2014, **158**, 391–399, DOI: 10.1016/j.apcatb.2014.04.049.
64 R. P. Ye, L. Lin, Q. Li, Z. Zhou, T. Wang, C. K. Russell, H. Adidharma, Z. Xu, Y. G. Yao and M. Fan, *Catal. Sci. Technol.*, 2018, **8**(14), 3428–3449, DOI: 10.1039/c8cy00608c.
65 L. Ma, H. Liu and D. He, *Bioengineering*, 2023, **10**, 1264, DOI: 10.3390/bioengineering10111264.
66 F. Cai, D. Pan, J. J. Ibrahim, J. Zhang and G. Xiao, *Appl. Catal., A*, 2018, **564**, 172–182, DOI: 10.1016/j.apcata.2018.07.029.
67 S. Liu, Z. Yu, C. Lu, Y. Wang, F. Sun, Z. Sun, Y. Liu, C. Shi and A. Wang, *Fuel*, 2023, **334**, 126763, DOI: 10.1016/j.fuel.2022.126763.
68 N. Azri, R. Irmawati, U. I. Nda-Umar, M. I. Saiman and Y. H. Taufiq-Yap, *J. King Saud Univ., Sci.*, 2021, **33**(4), 101417, DOI: 10.1016/j.jksus.2021.101417.
69 C. Wang, H. Jiang, C. Chen, R. Chen and W. Xing, *Chem. Eng. J.*, 2015, **264**, 344–350, DOI: 10.1016/j.cej.2014.11.113.
70 S. M. Pudi, P. Biswas, S. Kumar and B. Sarkar, *J. Braz. Chem. Soc.*, 2015, **26**(8), 1551–1564, DOI: 10.5935/0103-5053.20150123.
71 J. B. Salazar, D. D. Falcone, H. N. Pham, A. K. Datye, F. B. Passos and R. J. Davis, *Appl. Catal., A*, 2014, **482**, 137–144, DOI: 10.1016/j.apcata.2014.06.002.
72 W. Yu, J. Zhao, H. Ma, H. Miao, Q. Song and J. Xu, *Appl. Catal., A*, 2010, **383**(1–2), 73–78, DOI: 10.1016/j.apcata.2010.05.023.
73 Z. Wu, Y. Mao, M. Song, X. Yin and M. Zhang, *Catal. Commun.*, 2013, **32**, 52–57, DOI: 10.1016/j.catcom.2012.12.006.
74 H. Tan, M. N. Hedhill, Y. Wang, J. Zhang, K. Li, S. Sioud, Z. A. Al-Talla, M. H. Amad, T. Zhan, O. E. Tall and Y. Han, *Catal. Sci. Technol.*, 2013, **3**(12), 3360–3370, DOI: 10.1039/c3cy00661a.
75 B. K. Kwak, D. S. Park, Y. S. Yun and J. Yi, *Catal. Commun.*, 2012, **24**, 90–95, DOI: 10.1016/j.catcom.2012.03.029.
76 S. M. Pudi, P. Biswas and S. Kumar, *J. Chem. Technol. Biotechnol.*, 2016, **91**(7), 2063–2075, DOI: 10.1002/jctb.4802.
77 A. S. Yusuff, A. K. Bhonsle, D. P. Bangwal and N. Atray, *Renew. Energy*, 2021, **177**, 1253–1264, DOI: 10.1016/j.renene.2021.06.039.
78 Y. Yang, M. Liu, X. You, Y. Li, H. Lin and J. P. Chen, *Chem. Eng. J.*, 2024, **479**, 147320, DOI: 10.1016/j.cej.2023.147320.
79 S. P. Gouda, D. Shi, S. Basumatary, H. Li, R. Piloto-Rodríguez and S. L. Rokhum, *Chem. Eng. J.*, 2024, **480**, 148154, DOI: 10.1016/j.cej.2023.148154.
80 A. Wołosiak-Hnat, E. Milchert and G. Lewandowski, *Org. Process Res. Dev.*, 2013, **17**(4), 701–713, DOI: 10.1021/op4000175.
81 X. Li, Q. Wang, Y. Wu, J. Chen, S. Li, Y. Ye, D. Wang and Z. Zheng, *Biomass Bioenergy*, 2022, **158**, 106379, DOI: 10.1016/j.biombioe.2022.106379.
82 F. Moghadaskhou, R. Eivazzadeh-Keihan, Z. Sadat, A. Tadjarodi and A. Maleki, *Sci. Rep.*, 2023, **13**(1), 16584, DOI: 10.1038/s41598-023-43869-2.
83 Á. B. Sifontes, B. Gutierrez, A. Mónaco, A. Yanez, Y. Díaz, F. J. Méndez, L. Llovera, E. Cañizales and J. L. Brito, *Biotechnol. Rep.*, 2014, **4**, 21–29, DOI: 10.1016/j.btre.2014.07.001.
84 A. Abdelkader, B. M. Hussien, E. M. Fawzy and A. A. Ibrahim, *Appl. Petrochem. Res.*, 2021, **2**, 137–146, DOI: 10.1007/s13203-021-00267-x.
85 J. P. da SQ Menezes, R. L. Manfro and M. M. V. M. Souza, *Int. J. Hydrogen Energy*, 2018, **43**(32), 15064–15082, DOI: 10.1016/j.ijhydene.2018.06.048.
86 A. J. Pamphile-Adrian, F. B. Passos and P. P. Florez-Rodriguez, *Catal. Today*, 2022, **394**, 499–509, DOI: 10.1016/j.cattod.2021.07.002.